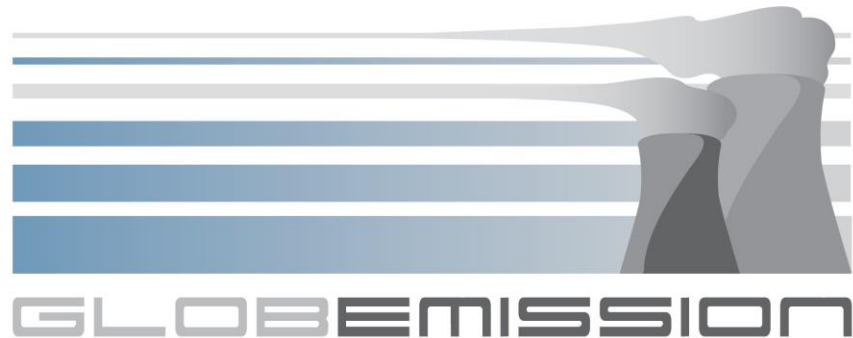




Title: Product Validation Report
Ref.: GE_PVR_04
Issue: 1.0
Date: 5 January 2016
Page: 1 of 41



GlobEmission

ESA Contract No 4000104001/11/I-NB

PRODUCT VALIDATION REPORT(v4)

Date of Issue : 5 January 2016



Title: Product Validation Report
Ref.: GE_PVR_04
Issue: 1.0
Date: 5 January 2016
Page: 2 of 41

<i>Lead Author</i>	Jenny Stavrakou (BIRA-IASB)
<i>Contributing Authors</i>	Maite Bauwens, Bas Mijling, Ronald van der A, Mikhail Sofiev, Julius Vira, Gerrit de Leeuw, Lyana Curier
<i>Reviewed by</i>	Claus Zehner, ESA
<i>Distribution List</i>	Claus Zehner, ESA, WP leaders, Public

Document Change record

<i>Date</i>	<i>Issue</i>	<i>Pages affected</i>	<i>Description</i>
<i>5 January 2016</i>	1.0	all	final



Table of Contents

1. Introduction	5
Purpose and scope.....	5
2. Documents	5
Reference documents.....	5
3. GLOBAL NMVOC FIRE EMISSIONS (BIRA-IASB).....	12
3.1 EVALUATION AGAINST EXISTING EMISSION INVENTORIES	12
3.2 EVALUATION AGAINST SATELLITE OBSERVATIONS	15
3.2.1 MODIS fire counts	15
3.2.2 GOME-2 HCHO columns	16
4. GLOBAL BIOGENIC ISOPRENE EMISSIONS (BIRA-IASB).....	17
4.1 EVALUATION AGAINST EXISTING EMISSION INVENTORIES	17
4.2 EVALUATION AGAINST SATELLITE OBSERVATIONS.....	19
4.3 EVALUATION AGAINST GROUND-BASED MEASUREMENTS.....	20
5. ANTHROPOGENIC VOC EMISSIONS OVER ASIA (BIRA-IASB).....	21
5.1 EVALUATION AGAINST EMISSION INVENTORIES	21
5.2 EVALUATION AGAINST SATELLITE OBSERVATIONS.....	22
5.3 EVALUATION AGAINST GROUND-BASED MEASUREMENTS.....	23
6. NO_x EMISSIONS AND TRENDS IN EUROPE (TNO).....	25
6.1 EVALUATION AGAINST SATELLITE OBSERVATIONS.....	25
6.2 EVALUATION AGAINST GROUND-BASED MEASUREMENTS.....	27
7. REGIONAL NO_x EMISSION INVENTORIES (KNMI)	28
7.1 The DECSO emission estimation algorithm overview	28
7.2 EVALUATION OF EAST ASIAN EMISSIONS AGAINST EXISTING INVENTORIES.....	29
7.2.1 MEIC inventory	29
7.2.2 South Korean CAPPs inventory.....	32



Title: Product Validation Report
Ref.: GE_PVR_04
Issue: 1.0
Date: 5 January 2016
Page: 4 of 41

7.3 EVALUATION OF MIDDLE EAST EMISSIONS AGAINST EXISTING INVENTORIES.....	33
7.4 EVALUATION OF SOUTH AFRICAN EMISSIONS AGAINST EXISTING INVENTORIES...35	
7.5 EVALUATION OF INDIAN EMISSIONS AGAINST EXISTING INVENTORIES.....	36
7.6 EVALUATION OF INDIAN EMISSIONS AGAINST SATELLITE OBSERVATIONS.....	36
7.7 INVENTORY ISSUES, FUTURE IMPROVEMENTS.....	37
8. IS4FIRES INVENTORY (FMI).....	38



1. INTRODUCTION

PURPOSE AND SCOPE

The fourth part of the validation of the satellite-derived emission inventories is carried out and discussed in this document. To that purpose, we use independent emission inventories, satellite datasets that have not been used in the derivation of the satellite-based emissions and ground-based measurements. More specifically, in this version of the validation report :

- The global GlobEmission NMVOC fire emissions are evaluated against the independent fire inventories FINNv1.5 [RD-Wiedinmyer2011], and GFAS [RD-Kaiser2012], the newly released GFED4 inventory (July 2015), as well as against fire counts from MODIS Aqua/Terra. Satellite columns of HCHO retrieved by GOME-2 instrument are used to evaluate the consistency of emissions derived from two satellite instruments. Furthermore, the global satellite-derived isoprene emissions are compared to two global inventories : MEGAN-MACC [RD-Sinderalova2014] and to GUESS-ES [RD-Arneth2007], as well as to a compilation of isoprene flux measurements in the Amazon region. Isoprene emissions constrained by OMI are further evaluated against GOME-2 derived emissions in 2010.
- On the regional scale, GlobEmission anthropogenic NO_x emissions over Asia are compared with the recent MEIC inventory, literature estimates, and with emissions from the CAPSS high-resolution inventory for South Korea. Anthropogenic VOC emissions over Asia are evaluated against the MEIC inventory for VOCs, with GOME-2 derived VOC estimates, and ground-based MAX-DOAS and FTIR measurements used to evaluate the model skill to reproduce the diurnal cycle of HCHO columns. The GlobEmission NO_x emission inventory over the Middle East is evaluated through comparisons with EDGARv4.2, and EDGARv4.3, over South Africa and India with EDGARv4.2 bottom-up inventory. European NO_x emissions and trends derived by OMI are compared to GOME-2 derived trends, and to ground-based measurements from AIRBASE.

2. DOCUMENTS

REFERENCE DOCUMENTS

[RD-PVPv1] GE_PVP_01.doc

[RD-PVRv1] GE_PVR_01.doc

[RD-PVRv2] GE_PVR_02.doc

[RD-PVRv3] GE_PVR_03.doc

[RD-PVPv2] GE_PVP_02.doc

[RD-ATBDv3] GlobEmission Algorithm Theoretical Baseline Document (ATBD), Issue 3.0 Rev. 3, 17 March 2015.

[RD-Alves2015] Alves, E. G., Jardine, K., Tóta, J., Jardine, A., Yáñez-Serrano, A. M., Karl, T., Tavares, J. V., Nelson, B., Gu, D., Stavrou, T., et al.: Seasonality of isoprenoid atmospheric vertical profiles within and above a primary rainforest in central Amazonia, *Atmos. Chem. Phys. Discuss.*, 15, 28867-28913, doi:10.5194/acpd-15-28867-2015, 2015.

[RD-Andela2013] Andela, N., Kaiser, J. W., Heil, A., Leeuwen, T. T. van, Werf, G. R. van der, Wooster, M. J., Remy, S. and Schultz, M. G.: Assessment of the Global Fire Assimilation System (GFASv1), MACC-II project (Monitoring Atmospheric Composition and Climate - Interim Implementation), 2013.

[RD-Andela2014] Andela, N. and van der Werf, G. R.: Recent trends in African fires driven by cropland expansion and El Niño to La Niña transition, *Nature Climate Change*, 4(9), 791–795, doi:10.1038/nclimate2313, 2014.

[RD-Anderson2015] Anderson, L. O., Aragão, L. E., Gloor, M., Arai, E., Adami, M., Saatchi, S., Malhi, Y., Shimabukuro, Y. E., Barlow, J., Berenguer, E., et al.: Disentangling the contribution of multiple land covers to fires-mediated carbon emissions in Amazonia during the 2010 drought, *Global Biogeochem. Cy.*, doi:10.1002/2014GB005008, 2015.

[RD-Arneth2007] Arneth, A., Niinemets, U., Pressley, S., Bck, J., Hari, P., Karl, T., Noe, S., Prentice, I., Serc, a, D., Hickler, T. et al. : Process-based estimates of terrestrial ecosystem isoprene emissions: incorporating the effects of a direct CO₂-isoprene interaction, *Atmos. Chem. Phys.*, 7(1), 31–53, doi:10.5194/acp-7-31-2007, 2007.

[RD-Ballhorn2009] Ballhorn, U., Siegert, F., Mason, M. and Limin, S.: Derivation of burn scar depths and estimation of carbon emissions with LIDAR in Indonesian peatlands, *Proc. Natl. Acad. Sci. U.S.A.*, 106(50), 21213–21218, doi:10.1073/pnas.0906457106, 2009.

[RD-Bessagnet20014] Bessagnet, B., A. Hodzic, R. Vautard, M. Beekmann, S. Cheinet, C. Honoré, C. Liousse, and L. Rouil (2004). Aerosol modeling with CHIMERE - preliminary evaluation at the continental scale, *Atmos. Environ.* 38, 2803–2817.

[RD-Bloom2015] Bloom, A. A., Worden, J., Jiang, Z., Worden, H., Kurosu, T., Frankenberg, C. and Schimel, D.: Remote-sensing constraints on South America fire traits by Bayesian fusion of atmospheric and surface data, *Geophys. Res. Lett.*, 42(4), 1268–1274, doi:10.1002/2014GL02584, 2015.

[RD-Boersma2011] Boersma, K.F., H.J. Eskes, R.J. Dirksen, R.J. van der A, J.P. Veefkind, P. Stammes, V. Huijnen, Q.L. Kleipool, M. Sneep, J. Claas, J. Leitao, A. Richter, Y. Zhou and D. Brunner, An improved tropospheric NO₂ column retrieval algorithm for the Ozone Monitoring Instrument, *Atmos. Meas. Tech.*, 2011, 4, 1905-1928, doi:10.5194/amt-4-1905-2011.

[RD-Chevallier2009] Chevallier, F., Fortems, A., Bousquet, P., Pison, I., Szopa, S., Devaux, M. and Hauglustaine, D.: African CO emissions between years 2000 and 2006 as estimated from MOPITT observations, *Biogeosciences*, 6(1), 103–111, doi:10.5194/bgd-5-3845-2008, 2009.

[RD-Ciccioli2003] Ciccioli, P., Brancaleoni, E., Frattoni, M., Kuhn, U., Kesselmeier, J., Dindorf, T., Araujo, A. de, Nobre, A., Stefani, P. and Valentini, R.: Fluxes of isoprenoid compounds over the tropical rainforest near Manaus during the dry season and their implications in the ecosystem carbon budget and in the atmospheric chemistry processes, in *Integrated Land Ecosystem–Atmosphere Processes Study (ILEAPS) International Open Science Conference 2003*, pp. 48–53, Finnish Association for Aerosol Research., 2003.

[RD-Coumou2012] Coumou, D. and Rahmstorf, S.: A decade of weather extremes, *Nature Climate Change*, 2(7), 491–496, doi:10.1038/nclimate1452, 2012.

[RD-De Smedt2012] De Smedt, I., Van Roozendaal, M., Stavrakou, T., Müller, J.-F., Lerot, C., Theys, N., Valks, P., Hao, N. and A. R. van der: Improved retrieval of global tropospheric formaldehyde columns from GOME-2/MetOp-A addressing noise reduction and instrumental degradation issues, *Atmos. Meas. Tech.*, 5(11), 2933–2949, doi:10.5194/amt-5-2933-2012, 2012.

[RD-De Smedt2015] De Smedt, I., Stavrakou, T., Hendrick, F., Danckaert, T., Vlemmix, T., Pinardi, G., Theys, N., Lerot, C., Gielen, C., Vigouroux, C., et al.: Diurnal, seasonal and long-term variations of global formaldehyde columns inferred from combined OMI and GOME-2 observations, *Atmos. Chem. Phys.*, 15(8), 12519–12545, doi:10.5194/acp-15-12519-2015, 2015.

[RD-EDGAR] European Commission, Joint Research Centre (JRC)/Netherlands Environmental Assessment Agency (PBL). Emission Database for Global Atmospheric Research (EDGAR), release version 4.0. <http://edgar.jrc.ec.europa.eu>, 2009.

[RD-Founda2009] Founda, D. and Giannakopoulos, C.: The exceptionally hot summer of 2007 in Athens, Greece—a typical summer in the future climate?, *Global and Planetary Change*, 67(3), 227–236, 2009.

[RD-Gielen2014] Gielen, C., Van Roozendaal, M., Hendrick, F., Pinardi, G., Vlemmix, T., De Bock, V., De Backer, H., Fayt, C., Hermans, C., Gillotay, D., et al.: A simple and versatile cloud-screening method for MAX-DOAS retrievals, *Atmos. Meas. Tech.*, 7(10), 3509–3527, 2014.

[RD-Giglio2013] Giglio, L., Randerson, J. T. and Werf, G. R.: Analysis of daily, monthly, and annual burned area using the fourth-generation global fire emissions database (GFED4), *J. Geophys. Res.-Biogeo.*, 118(1), 317–328, doi:10.1002/jgrg.20042, 2013.

[RD-Gorchakov2014] Gorchakov, G., Sitnov, S., Sviridenkov, M., Semoutnikova, E., Emilenko, A., Isakov, A., Kopeikin, V., Karpov, A., Gorchakova, I., Verichev, K., et al.: Satellite and ground-based monitoring of smoke in the atmosphere during the summer wildfires in European Russia in 2010 and Siberia in 2012, *Int. J. Remote Sens.*, 35(15), 5698–5721, doi:10.1080/01431161.2014.945008, 2014.

[RD-Griffiths2007] Griffiths, P. R. and De Haseth, J. A.: *Fourier transform infrared spectrometry*, John Wiley & Sons, Hoboken, New Jersey, USA., 2007.

[RD-He2012] He, K.: Multi-resolution Emission Inventory for China (MEIC): model framework and 1990–2010 anthropogenic emissions, in: International Global Atmospheric Chemistry Conference, 17–21 September, Beijing, China, available at: <http://adsabs.harvard.edu/abs/2012AGUFM.A32B..05H> (last access: 4 February 2015), 2012.

[RD-Helmig1998] Helmig, D., Balsley, B., Davis, K., Kuck, L. R., Jensen, M., Bogner, J., Smith, T., Arrieta, R. V., Rodriguez, R. and Birks, J. W.: Vertical profiling and determination of landscape fluxes of biogenic nonmethane hydrocarbons within the planetary boundary layer in the Peruvian Amazon, *J. Geophys. Res.-Atmos.*, 103(D19), 25519–25532, 1998.

[RD-Hendrick2014] Hendrick, F., Müller, J.-F., Clémer, K., Wang, P., Mazière, M. D., Fayt, C., Gielen, C., Hermans, C., Ma, J., Pinardi, G., et al.: Four years of ground-based MAX-DOAS observations of HONO and NO₂ in the Beijing area, *Atmos. Chem. Phys.*, 14(2), 765–781, 2014.

[RD-Hönninger2004] Hönninger, G., Friedeburg, C. von and Platt, U.: Multi axis differential optical absorption spectroscopy (MAX-DOAS), *Atmos. Chem. Phys.*, 4(1), 231–254, 2004.

[RD-JRC2015] Joint Research Centre (JRC), HTAP_V2 inventory, http://edgar.jrc.ec.europa.eu/htap_v2/index.php, 2014. Last accessed Dec 1, 2015.

[RD-Kaiser2012] Kaiser, J., Heil, A., Andreae, M., Benedetti, A., Chubarova, N., Jones, L., Morcrette, J.-J., Razinger, M., Schultz, M., Suttie, M. and others: Biomass burning emissions estimated with a global fire assimilation system based on observed fire radiative power., *Biogeosciences*, 9, 527–554, 2012.

[RD-Karl2007] Karl, T., Guenther, A., Yokelson, R. J., Greenberg, J., Potosnak, M., Blake, D. R. and Artaxo, P.: The tropical forest and fire emissions experiment: Emission, chemistry, and transport of biogenic volatile organic compounds in the lower atmosphere over Amazonia, *J. Geophys. Res.-Atmos.*, 112(D18), doi:10.1029/2007JD008539, 2007.

[RD-Koelemeijer2001] Koelemeijer, R., P. Stammes, J. Hovenier, and J. de Haan: A fast method for retrieval of cloud parameters using oxygen A band measurements from the global ozone monitoring experiment, *J. Geophys. Res.* 106, 3475–3490, 2001.

[RD-Konovalov2011] Konovalov, I., Beekmann, M., Kuznetsova, I., Yurova, A. and Zvyagintsev, A.: Atmospheric impacts of the 2010 Russian wildfires: integrating modelling and measurements of an extreme air pollution episode in the Moscow region, *Atmos. Chem. Phys.*, 11(19), 10031–10056, doi:10.5194/acp-11-10031-2011, 2011.

[RD-Krol2013] Krol, M., Peters, W., Hooghiemstra, P., George, M., Clerbaux, C., Hurtmans, D., McInerney, D., Sedano, F., Bergamaschi, P., Hajj, M. E., et al.: How much CO was emitted by the 2010 fires around Moscow?, *Atmos. Chem. Phys.*, 13(9), 4737–4747, doi:10.5194/acp-13-4737-2013, 2013.

[RD-Kuhn2007] Kuhn, U., Andreae, M., Ammann, C., Araújo, A., Brancaleoni, E., Ciccioli, P., Dindorf, T., Frattoni, M., Gatti, L., Ganzeveld, L., et al.: Isoprene and monoterpene fluxes from Central Amazonian rainforest inferred from tower-based and airborne measurements, and

implications on the atmospheric chemistry and the local carbon budget, *Atmos. Chem. Phys.*, 7(11), 2855–2879, doi:10.5194/acp-7-2855-2007, 2007.

[RD-Kurokawa2013] Kurokawa, J., Ohara, T., Morikawa, T., Hanayama, S., Greet, J.-M., Fukui, T., Kawashima, K. and Akimoto, H.: Emissions of air pollutants and greenhouse gases over Asian regions during 2000-2008: Regional Emission inventory in ASia (REAS) version 2, *Atmos. Chem. Phys.*, 13, 11019-11058, 2013.

[RD-Langford2010] Langford, B., Misztal, P., Nemitz, E., Davison, B., Helfter, C., Pugh, T., MacKenzie, A., Lim, S. and Hewitt, C.: Fluxes and concentrations of volatile organic compounds from a South-East Asian tropical rainforest., *Atmos. Chem. Phys.*, 10(17), doi:10.5194/acp-10-8391-2010, 2010.

[RD-Mijling2009] Mijling, B., R.J. van der A, K.F. Boersma, M. Van Roozendael, I. De Smedt and H.M. Kelder: Reduction of NO₂ detected from space during the 2008 Beijing Olympic Games, *Geophys. Res. Lett.*, 36, doi:10.1029/2009GL038943, 2009.

[RD-Mijling2012] Mijling, B. and R.J. van der A: Using daily satellite observations to estimate emissions of short-lived air pollutants on a mesoscopic scale, *J. Geophys. Res.*, 117, doi:10.1029/2012JD017817, 2012.

[RD-Mijling2013] Mijling, B., R.J. van der A, R. J., and Q. Zhang: Regional nitrogen oxides emission trends in East Asia observed from space, *Atmos. Chem. Phys.* 13, 12003-12012, doi:10.5194/acp-13-12003-2013, 2013.

[RD-Niinemets1999] Niinemets, U., Tenhunen, J., Harley, P. and Steinbrecher, R. : A model of isoprene emission based on energetic requirements for isoprene synthesis and leaf photosynthetic properties for Liquidambar and Quercus, *Plant, Cell Environ.*, 22(11), 1319–1335, doi:10.1046/j.1365-3040.1999.00505.x, 1999.

[RD-Pétron2004] Pétron, G., Granier, C., Khattatov, B., Yudin, V., Lamarque, J.-F., Emmons, L., Gille, J. and Edwards, D. P.: Monthly CO surface sources inventory based on the 2000–2001 MOPITT satellite data, *Geophys. Res. Lett.*, 31(21), 2004.

[RD-Platt2008] Platt, U. and Stutz, J.: *Differential absorption spectroscopy*, Springer, Berlin, Heidelberg, Germany, 2008.

[RD-Randerson2012] Randerson, J., Chen, Y., Werf, G., Rogers, B. and Morton, D.: Global burned area and biomass burning emissions from small fires, *J. Geophys. Res.-Biogeo.*, 117(G4), doi:10.1029/2012JG002128, 2012.

[RD-Reddington2014] Reddington, C., Yoshioka, M., Balasubramanian, R., Ridley, D., Toh, Y., Arnold, S. and Spracklen, D.: Contribution of vegetation and peat fires to particulate air pollution in Southeast Asia, *Environ. Res. Lett.*, 9(9), 094006, 2014.

[RD-Simon2005] Simon, E., Meixner, F., Rummel, U., Ganzeveld, L., Ammann, C. and Kesselmeier, J.: Coupled carbon-water exchange of the Amazon rain forest, II. Comparison of predicted and

observed seasonal exchange of energy, CO₂, isoprene and ozone at a remote site in Rondônia, Biogeosciences Discuss., 2(2), 399–449, doi:10.5194/bg-2-255-2005, 2005.

[RD-Sitch2003] Sitch, S., Smith, B., Prentice, I. C., Arneth, A., Bondeau, A., Cramer, W., Kaplan, J., Levis, S., Lucht, W., Sykes, M. T. et al. : Evaluation of ecosystem dynamics, plant geography and terrestrial carbon cycling in the LPJ dynamic global vegetation model, *Global Change Biology*, 9(2), 161–185, doi:10.1046/j.1365-2486.2003.00569.x, 2003.

[RD-Sinderalova2014] Sindelarova, K., C. Granier, I. Bouarar, A. Guenther, S. Tilmes, T. Stavrakou, J.-F. Müller, U. Kuhn, P. Stefani, and W. Knorr, Global dataset of biogenic VOC emissions calculated by the MEGAN model over the last 30 years, *Atmos. Chem. Phys.*, 14, 9317–9341, 2014.

[RD-Schmidt2001] Schmidt, H., C. Derognat, R. Vautard, and M. Beekmann : A comparison of simulated and observed ozone mixing ratios for the summer of 1998 in Western Europe. *Atmos. Environ.* 36, 6277–6297, 2001.

[RD-Soares2015] Soares, J. M. Sofiev, J. Hakkarainen : Uncertainties of wild-land fires emissions in AQMEII phase 2 case study, *Atmos. Environ.*, doi:10.1016/j.atmosenv.2015.01.068, 2015.

[RD-Stavrakou2009] Stavrakou, T., Müller, J.-F., De Smedt, I., Van Roozendaal, M., Werf, G. R. van der, Giglio, L. and Guenther, A.: Evaluating the performance of pyrogenic and biogenic emission inventories against one decade of space-based formaldehyde columns, *Atmos. Chem. Phys.*, 9(3), 1037–1060, doi:10.5194/acp-9-1037-2009, 2009.

[RD-Stavrakou2014] Stavrakou, T., Müller, J.-F., Bauwens, M., De Smedt, I., Van Roozendaal, M., Guenther, A., Wild, M. and Xia, X.: Isoprene emissions over Asia 1979 - 2012: impact of climate and land-use changes, *Atmos. Chem. Phys.*, 14(9), 4587–4605, doi:10.5194/acp-14-4587-2014, 2014.

[RD-Stavrakou2015] Stavrakou, T., Müller, J.-F., Bauwens, M., De Smedt, I., Van Roozendaal, M., De Mazière, M., Vigouroux, C., Hendrick, F., George, M., Clerbaux, C., et al.: How consistent are top-down hydrocarbon emissions based on formaldehyde observations from GOME-2 and OMI? *Atmos. Chem. Phys.*, 15(8), 11861–11884, doi:10.5194/acp-15-11861-2015, 2015.

[RD-Turquety2009] Turquety, S., Hurtmans, D., Hadji-Lazaro, J., Coheur, P.-F., Clerbaux, C., Josset, D. and Tsamalis, C.: Tracking the emission and transport of pollution from wildfires using the IASI CO retrievals: analysis of the summer 2007 Greek fires, *Atmos. Chem. Phys.*, 9(14), 4897–4913, doi:10.5194/acp-9-4897-2009, 2009.

[RD-Vigouroux2009] Vigouroux, C., Hendrick, F., Stavrakou, T., Dils, B., Smedt, I. D., Hermans, C., Merlaud, A., Scolas, F., Senten, C., Vanhaelewyn, G., et al.: Ground-based FTIR and MAX-DOAS observations of formaldehyde at Réunion Island and comparisons with satellite and model data, *Atmos. Chem. Phys.*, 9(24), 9523–9544, 2009.

[RD-Vlemmix2015] Vlemmix, T., Hendrick, F., Pinardi, G., Smedt, I. D., Fayt, C., Hermans, C., PETERS, A., Wang, P., Levelt, P. and Roozendaal, M. V.: MAX-DOAS observations of aerosols,



formaldehyde and nitrogen dioxide in the Beijing area: comparison of two profile retrieval approaches, *Atmos. Meas. Tech.*, 8(2), 941–963, 2015.

[RD-Wiedinmyer2011] Wiedinmyer, C., Akagi, S., Yokelson, R., Emmons, L., Al-Saadi, J., Orlando, J. and Soja, A.: The Fire INventory from NCAR (FINN): A high resolution global model to estimate the emissions from open burning, *Geosci. Mod. Dev.*, 4(3), 625–641, doi:10.5194/gmd-4-625-2011, 2011.

[RD-Yurganov2011] Yurganov, L., Rakitin, V., Dzhola, A., August, T., Fokeeva, E., George, M., Gorchakov, G., Grechko, E., Hannon, S., Karpov, A., et al.: Satellite-and ground-based CO total column observations over 2010 Russian fires: accuracy of top-down estimates based on thermal IR satellite data, *Atmos. Chem. Phys.*, 11(15), 7925–7942, 2011.

[RD-Zhang2009] Zhang, Q., Streets, D. G., Carmichael, G. R., He, K. B., Huo, H., Kannari, A., Klimont, Z., Park, I. S., Reddy, S., Fu, J. S., Chen, D., Duan, L., Lei, Y., Wang, L. T., and Yao, Z. L.: Asian emissions in 2006 for the NASA INTEX-B mission, *Atmos. Chem. Phys.*, 9, 5131–5153, doi: 10.5194/acp-9-5131-2009, 2009.

3. GLOBAL NMVOC FIRE EMISSIONS (BIRA-IASB)

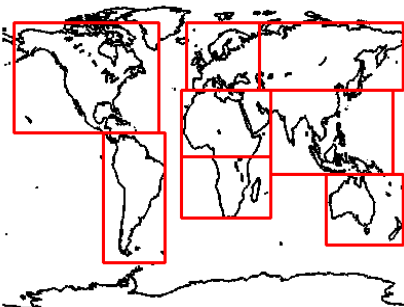
3.1 EVALUATION AGAINST EXISTING EMISSION INVENTORIES

The OMI-based fire emission estimates derived between 2005 and 2013 are compared with two independent inventories GFAS [RD-Kaiser2012] and FINNv1.5 [RD-Wiedinmyer2011], and with the latest GFED inventories GFED4 and GFED4s [RD-Randerson2012]. A full description of these inventories is found in the GlobEmission Product Validation Plan [GE-PVP-02].

The average global fire emission drops from 1886 TgC/yr (GFED3) to 1559 TgC/yr after inversion. The strongest emission decreases are induced over South America (38%), Northern Africa (33%) and Southeast Asia (29%), whereas in temperate regions the fire fluxes are generally higher than in GFED3, especially in Europe (25%). The top-down emission reduction is well in line with the GFED4 inventory (1438 TgC/yr), but the other three inventories (GFAS, FINNv1.5 and GFED4s) estimate larger globally averaged emissions (1938, 2006 and 2026 TgC/yr respectively). In the large regions of Table 1, the updated emissions agree well with GFED4 (average bias of 10%), and are in reasonable agreement with the estimates from the three other inventories, although there is an average positive bias of 20-38%. The lower top-down emissions in Africa are partly supported by GFED4, GFAS and FINNv1.5 inventories, and the positive flux increments in Europe, are in line with all other inventories (Figure 2). However, over tropical latitudes (Southeast Asia, Australia, South America), the estimates from the independent inventories exhibit often large discrepancies, and the top-down emissions are found to lie within their range (Figure 2).

Table 1. Definition of large regions in GlobEmission.

Region	Coordinates (lat - lon)	
N. America	13-75 N	40-170 W
S. America	60 S-13 N	90 W-35 E
Europe	37-75 N	15 W-50 E
N. Africa	0-37 N	20 W-65 E
S. Africa	0-35 S	20 W-55 E
Russia	37-75 N	50 -179 E
S.E. Asia	10 S-37 N	65-170 E
Australia	10-50 S	110-179 E



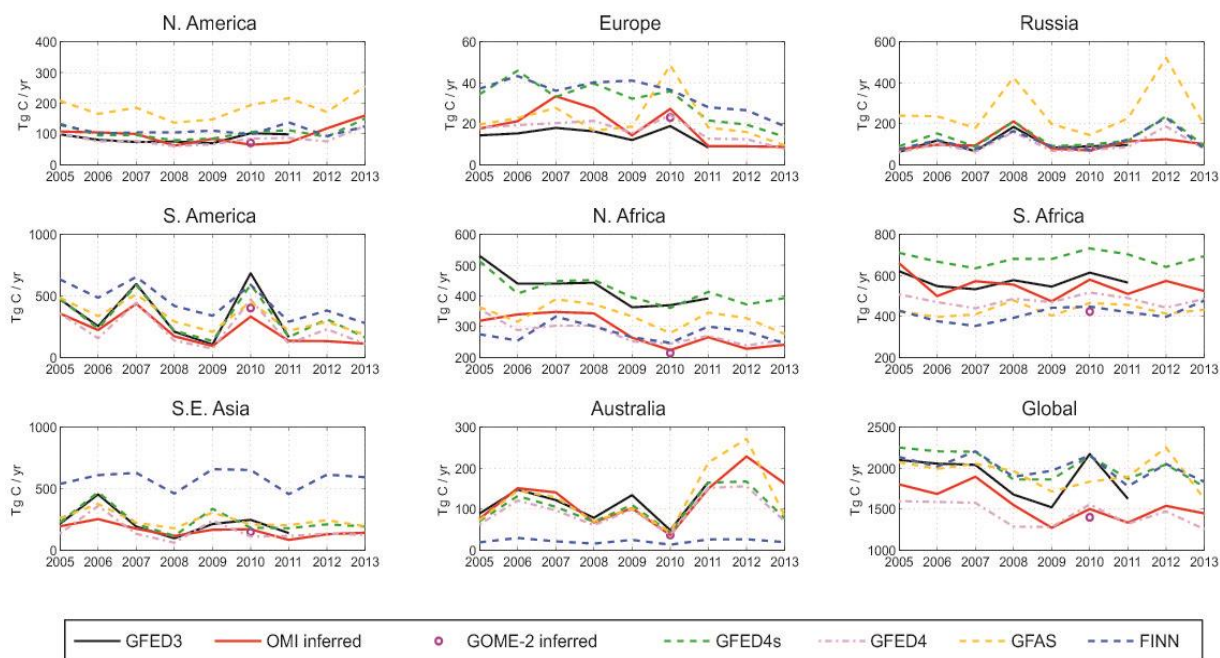


Figure 2. Annual bottom-up and top-down biomass burning emission estimates between 2005 and 2013 over the regions defined in Table 1. Units are in TgC per year.

Over South America the top-down interannual variability is marked, but less pronounced compared to the a priori, with the lowest emission inferred in 2009 (92 TgC) and the highest in 2007 (436 TgC). The resulting weaker interannual variability is in better agreement with the independent inventories, as confirmed by the higher a posteriori correlation with GFAS and FINN inventories (0.94 and 0.93, respectively), whereas the correlation with GFED4 and GFED4s remains higher than 0.95. The observations suggest substantial flux decreases in years with strong a priori fluxes, by 25% in 2005, by 27% in 2007 and by 52% in 2010. The strong flux reduction in 2010 is corroborated by inversion studies constrained by GOME-2 HCHO columns (-41%, [RD-Stavrakou2015]), by MOPITT CO observations (-28%, [RD-Bloom2015]), and by a multi-sensor based emission estimate above Mato Grosso (-60%, [RD-Anderson2015]). The overestimated GFED3 emissions during extreme drought episodes are likely due to the use in GFED3 model of fire persistence as a proxy for deforestation fires, leading thus to higher estimates than for forest fires only [RD-Anderson2015].

The top-down emission reduction of 20-40% derived for all years over Northern Africa brings the fluxes closer to GFED4, GFAS and FINN estimates (Figure 2). A decreasing trend of about 5.5%/yr over the study period is derived for the OMI-based fluxes (Figure 2), which is slightly higher than in GFED3 (-5.3%/yr) over 2005-2011. This negative trend is induced by the trends in the bottom-up GFED3 inventory and in the OMI columns (-0.84%/yr) and is related to negative trends observed in burned area in Northern Africa [RD-Andela2014; RD-Giglio2013] attributed to land use changes (conversion of savannah into cropland), and to changes in precipitation, driven by the El Niño/Southern Oscillation [RD-Andela2014].

In southern Africa, the OMI-based fluxes range between a minimum flux of 473 TgC in 2009 and a maximum of 660 TgC/yr in 2005, and are similar but somewhat lower than GFED3. The top-down fluxes are by 10-25% higher compared to the estimates of GFED4, GFAS and FINN (Figure 2) and by 20% lower than GFED4s [RD-Randerson2012]. The inversion infers 20% lower emissions in the beginning of the fire season, when fires are predominantly natural, and by ca. 30% higher emissions than GFED3 in September and October, when agricultural fires are more important. This seasonality shift of the burning season was also reported past inversion studies constrained by SCIAMACHY and GOME-2 HCHO [RD-Stavrakou2009, 2015] and MOPITT CO observations [RD-Chevallier2009], whereas an 1-2 month delay in the fire peak between the MODIS fire peak and MOPITT CO observations was already found in [RD-Pétron2004].

	North America	South America	Europe	Northern Africa	Southern Africa	Russia	Southeast Asia	Australia	Global
Biomass burning emissions (Tg C/yr)									
GFED3	85	355	15	426	572	99	222	112	1886
OMI-based	97	221	19	286	549	106	158	124	1559
GFAS	187	328	22	333	431	264	246	126	1938
FINNv1.5	112	452	34	278	415	114	579	22	2006
GFED4s	105	319	31	417	683	130	236	104	2026
GFED4	84	231	17	279	479	97	156	95	1438

Table 2. Mean a priori and OMI-based emission estimates compared to independent emission inventories for open biomass burning fluxes calculated for different world regions and globally. The means are taken over the period of data availability. Regions are defined as in Table 1. The means are calculated over 2005-2013 for all inventories, except for GFED3 (2005-2011) due to lack of data after 2011.

Over southeastern Asia the emission updates differ strongly among the years over the study period and lie between 82.3 TgC in 2011 and 252.2 TgC in 2006. They remain generally close to the initial inventory, except in 2006 where the GFED3 emissions associated to Indonesian peat fires [RD-Reddington2014] are almost halved after inversion (Figure 2). The lower 2006 flux suggested by the satellite is corroborated by an independent carbon emission estimate based on burned area field estimates for Central Kalimantan in 2006 [RD-Ballhorn2009], reporting peat fire emissions of 49 TgC, about twice lower than the GFED3 estimate (135 TgC), and closer to our estimate of 39 TgC for the same area.

At mid- and high-latitudes the OMI-based emissions remain generally close to the initial inventory and to most independent inventories (Figure 2, Table 2). The top-down annual estimates agree generally well with the independent bottom-up inventories, except for the discrepancy with GFAS in North America and Russia (factor of 2) and with FINN in Australia (factor of 4). The satellite observations point to factor of 2 increase with regard to GFED3 fluxes during the intense fire events that occurred in southern Europe during the summer 2007 heat wave, in line with the emission increases suggested by IASI CO columns [RD-Turquety2009]. A flux increase by 25% is also inferred during the devastating fires in the Moscow area in July-August 2010, which is supported by the estimated flux based on GOME-2 HCHO observations

[RD-Stavrou2015], and by the independent inventories. The OMI-based fluxes are lower, however, than previously reported values which were factor 2 [RD-Yurganov2011] and 3 [RD-Konovalov2011] higher than GFED3. Note also that an even stronger enhancement (up to factor of 10) of fire emissions with respect to GFED3 was reported during the Russian fires using assimilation of CO columns from IASI [RD-Krol2013].

3.2 EVALUATION AGAINST SATELLITE OBSERVATIONS

3.2.1 MODIS fire counts

To investigate whether the OMI-based product yields a better representation of small fire emissions we compare a priori and a posteriori emission estimates directly to MODIS fire counts on a monthly basis. To this aim, the monthly MODIS Aqua (MYD14CM, 13h30 LT) fire product is used. Twelve regions were defined based on literature studies regarding the occurrence of small fires, as displayed in Figure 3. The correlation coefficients calculated for the monthly time series are generally higher after the inversion, especially over regions undergoing extensive deforestation like Indochina where the correlation coefficient is improved from 0.78 to 0.94. In agricultural regions, like Southeastern US, the correlation coefficient is also higher after inversion, from 0.35 to 0.53, while increased correlations with the MODIS fire counts are also found over regions often experiencing peat fires, like Russia and Indonesia [RD-Andela2013]. Therefore, despite the fact that the initial inventory does not adequately account for small fires, the satellite-based results demonstrate skill in the representation of small fires, which is however limited, as demonstrated in the next paragraph by comparing the spatial distribution of the MODIS fire counts directly to the OMI HCHO observations.

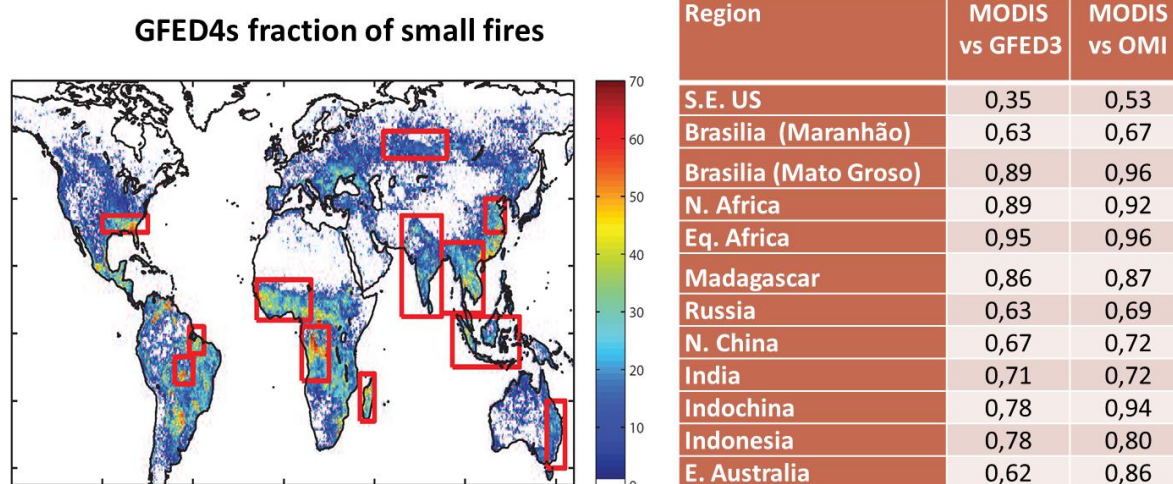


Figure 3. Left : regions selected based on the occurrence of small fires based on GFED4s. The map illustrates the annual fraction of small fires according to GFED4s. Right : Correlation coefficient between MODIS fire counts, GFED4 and OMI-based fluxes.

As shown in Figure 4 enhanced HCHO columns are observed in November over Maranhão (northeastern Brazil) and Mato Grosso (central Brazil), in accordance with the spatial

distribution of the MODIS fire counts. The inversion, however, falls short in reproducing the enhanced satellite columns in these regions, principally due to the fact that the a priori inventory lacks small fires. The underestimation of emissions from small fires in GFED3 is a recognized problem, which has been amended in the new GFED4s inventory. However, as illustrated in Figure 4, although the GFED4s estimate is factor of two higher than GFED3 in the Amazon, it is 4 times lower than the GFAS estimate for the same region and month. Despite the remaining underestimation in November compared to GFAS, the optimization reproduces slightly better the temporal variation of the MODIS fire counts over Maranhão and Mato Grosso (Figure 4).

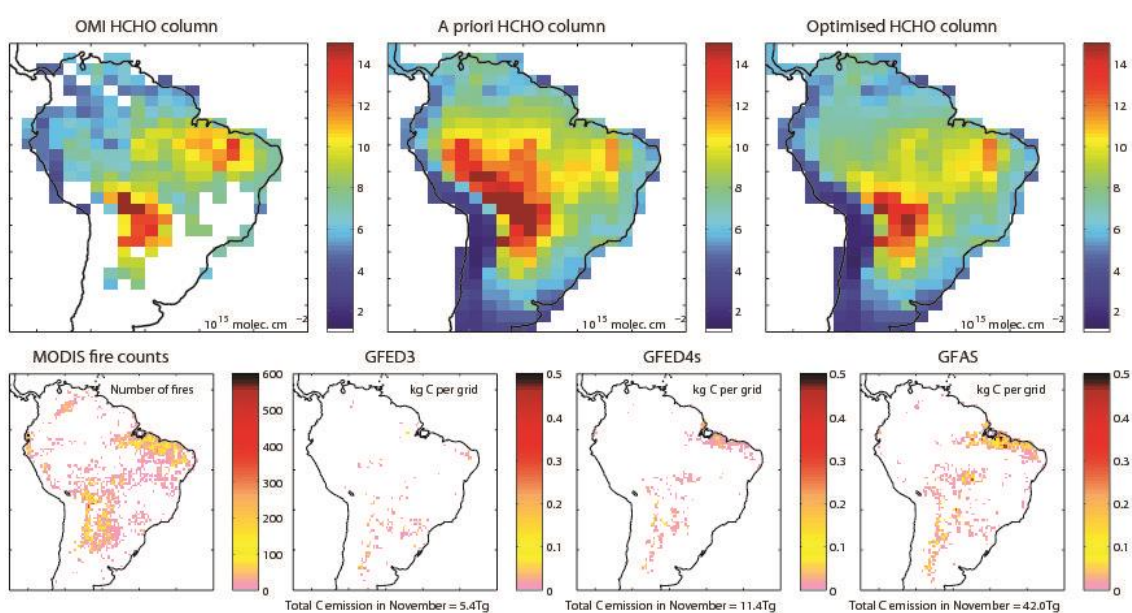


Figure 4. Amazon in November 2010 (upper panel from left to right) HCHO column observations by OMI, a priori modelled and optimized HCHO columns. Lower panel from left to right : MODIS fire counts, GFED3, GFED4s and GFAS emissions.

3.2.2 GOME-2 HCHO columns

The vertical columns of formaldehyde retrieved from two satellite instruments, the GOME-2 on Metop-A and the OMI on Aura, are used to constrain global emissions of HCHO precursors from open fires, vegetation and human activities in the year 2010. The current version (v14) of the HCHO retrievals applied to GOME-2/Metop-A and OMI/Aura measurements is based on the algorithm developed for GOME-2 (version 12, [RD-DeSmedt2012]), with significant adaptations, as detailed in [RD-De Smedt2015]. In general the early afternoon columns of OMI are higher than the mid-morning values of GOME-2 at mid-latitudes, while the reverse is true at most tropical locations [RD-De Smedt2015].

After inversion, the consistency between the top-down VOC emissions is highest in tropical regions (Figure 5). Both GOME-2 and OMI inversions suggest a strong decrease in global biomass burning VOC emissions with regard to the a priori GFEDv3 inventory, by 36 and 33 %, respectively. This decrease is most pronounced in tropical regions. The fire burning estimates

from the two inversions are generally quite consistent, not only globally but also over large emitting regions like Amazonia, southeastern Asia, and Africa. Both OMI and GOME-2 optimizations lead to enhanced emissions (by about 50 %) due to the extensive fires which plagued European Russia in August 2010 and to agricultural waste burning in the North China Plain in June.

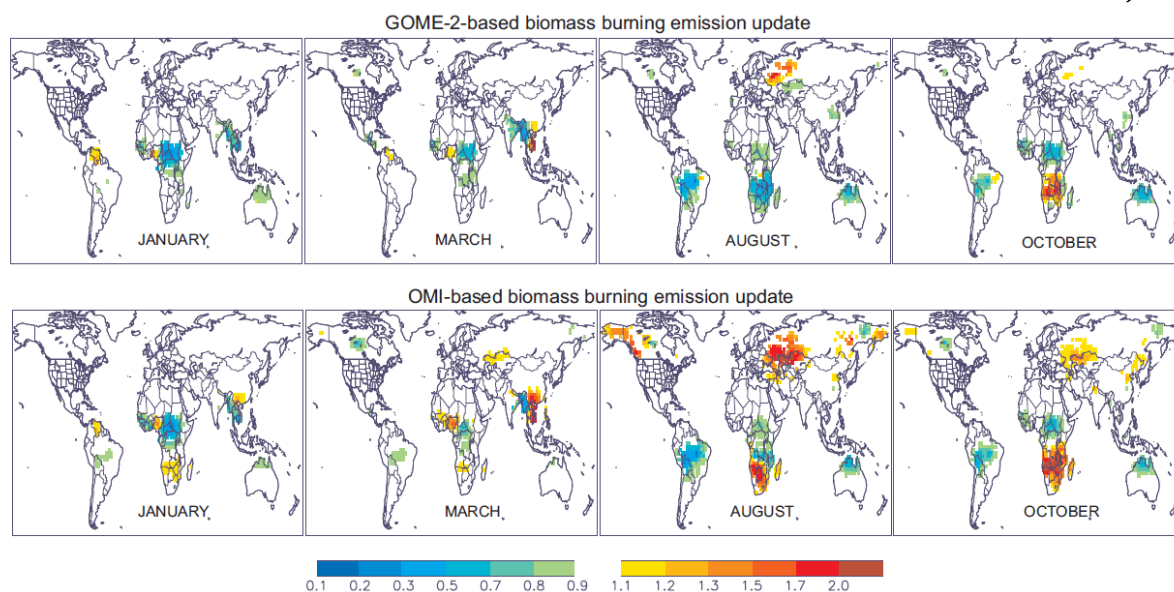


Figure 5. Ratios of optimized to a priori pyrogenic VOC fluxes derived by source inversion of HCHO columns from GOME-2 (upper panels) and OMI (lower panels) in January, March, August and October 2010. Ratio values between 0.9 and 1.1 are not shown for the sake of clarity.

4. GLOBAL BIOGENIC ISOPRENE EMISSIONS (BIRA-IASB)

4.1 EVALUATION AGAINST EXISTING EMISSION INVENTORIES

The global annual 2005-2013 isoprene emission averaged over 2005-2013 is reduced from 343 to 307 Tg after inversion (Figure 6). In comparison with the a priori MEGAN-MOHYCANv2 inventory, the global mean fluxes decrease by 10%, in good agreement with the reduction inferred by GOME-2 HCHO observations in 2010 [RD-Stavrakou2015]. As opposed to the emission decrease suggested by satellite, the average isoprene emission estimates from the MEGAN-MACC and GUESS-ES inventories are substantially higher than the top-down values, by 86% and by 47%, respectively. The MEGAN-MACC inventory relies on the MEGANv2.1 model for biogenic volatile organic compounds (BVOC) [RD-Sinderalova2014]. The emissions are provided at $0.5^\circ \times 0.5^\circ$ resolution and on a monthly basis from 1979 through 2010. The GUESS-ES isoprene inventory is based on the physiological isoprene emission algorithm described by [RD-Niinemets1999] and updated by [RD-Arneth2007]. It is coupled to the dynamic global vegetation model LPJ-GUESS [RD-Sitch2003] and is driven by the CRU (Climatic Research Unit) monthly meteorological fields (Mitchell and Jones, 2005) at $1^\circ \times 1^\circ$ resolution between 1969 and 2009. Both inventories are available at the ECCAD data portal (<http://eccad.sedoo.fr>).

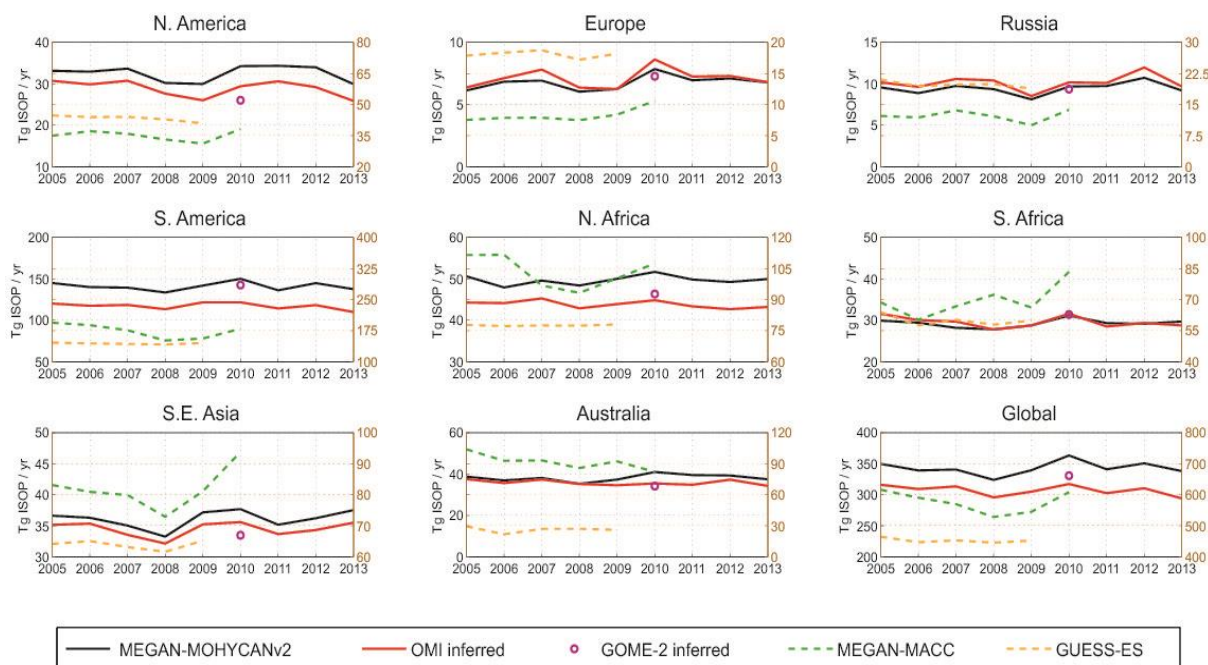


Figure 6. Mean Annual bottom-up and top-down isoprene emission estimates between 2005 and 2013 over the regions defined in Table 1. For convenience, a different scale is used for the emission estimates from MEGAN-MACC and GUESS-ES on the right end of each panel. Units are in TgC per year.

Table 3. Mean a priori and OMI-based emission estimates compared to independent inventories for isoprene fluxes. The means are taken over the period of data availability. Regions are defined as in Table 1. The means are calculated over 2005-2013 for all inventories, except for MEGAN-MACC (2005-2010), GUESS-ES (2005-2009) due to lack of data.

	North America	South America	Europe	Northern Africa	Southern Africa	Russia	Southeast Asia	Australia	Global
Isoprene emissions (Tg isoprene/yr)									
MEGAN MOHYCANv2	32	141	6.8	50	29	9	36	38	343
OMI-based	29	117	7.1	44	30	10	34	36	307
MEGAN-MACC	34	173	8.3	103	67	12	80	94	570
GUESS-ES	44	143	18.1	78	59	20	63	26	451

In the Tropics, the emissions are systematically decreased under the effect of the optimization (Table 3), by 17% and 12% on average over South America and Northern Africa, respectively, whereas the reductions are much stronger locally (up 40% in the Amazon, and up to 25% in equatorial Africa), pointing to potentially overestimated emission factors used in the MEGAN model for the tropical forests. In contrast to these regions, the emission reduction for the

tropical rainforests of South Asia is weak (<10%). This is explained by the fact that the a priori MEGAN-MOHYCANv2 [RD-Stavrakou2014] accounts for isoprene flux rates measured during the OP3 campaign in the rainforest of Borneo [RD-Langford2010], which are factor of 4 lower than assumed in the standard MEGAN parameterization. The good agreement between a priori model predictions and the satellite HCHO columns in Southeast Asia clearly supports the use of lower isoprene flux rates for the Asian rainforests.

In the temperate forests of Europe and Russia HCHO observations suggest larger fluxes during extreme heat waves, like in eastern Europe in 2007 and 2010 and in Siberia in 2012. Compared to the average emission increase of 4% in Europe, the optimized solution indicates significantly stronger emission increases in July 2007 over Southeastern Europe (+32%) and in July 2010 over European Russia near Moscow (+30%). In July 2007 Greece experienced the hottest summer on record since 1891 [RD-Founda2009] with temperature anomalies of 5°C compared to the 1961-1990 mean, whereas the hottest summer in Western Russia since 1500 was recorded in 2010 with temperature anomalies of +6°C with respect to the 1961-1990 mean ([RD-Coumou2012], <http://www.ncdc.noaa.gov/temp-and-precip>). Similarly, over Siberia in 2012 the updated emissions are locally increased by 47% (Figure 6), responding to high HCHO columns associated with an extremely warm summer, where the average annual air temperature in June exceeded by 7°C the 1961-1990 mean for this region (<http://www.ncdc.noaa.gov/tempand-precip/>). The heat waves mentioned above were accompanied by devastating fires [RD-Gorchakov2014; RD-Turquety2009].

4.2 EVALUATION AGAINST SATELLITE OBSERVATIONS

The vertical columns of formaldehyde retrieved from the GOME-2 instrument are used to constrain the global emissions of isoprene in 2010. The current version (v14) of the HCHO retrievals applied to GOME-2/Metop-A measurements is based on the algorithm developed for GOME-2 (version 12, [RD-DeSmedt2012]), with significant adaptations, as detailed in [RD-DeSmedt2015]. In general the early afternoon columns of OMI are higher than the mid-morning values of GOME-2 at mid-latitudes, while the reverse is true at most tropical locations [RD-DeSmedt2015].

The isoprene fluxes derived from this inversion are compared to the fluxes from the standard products based on OMI HCHO columns. The emissions are generally reduced globally, by 9% according to GOME-2 and by 13% according to OMI, compared to the a priori estimate of the MEGAN-ECMWF-v2 inventory (363.1 Tg/yr). The overall consistency between the global estimates is high for this emission category, despite some significant differences at a regional scale (Figure 7).

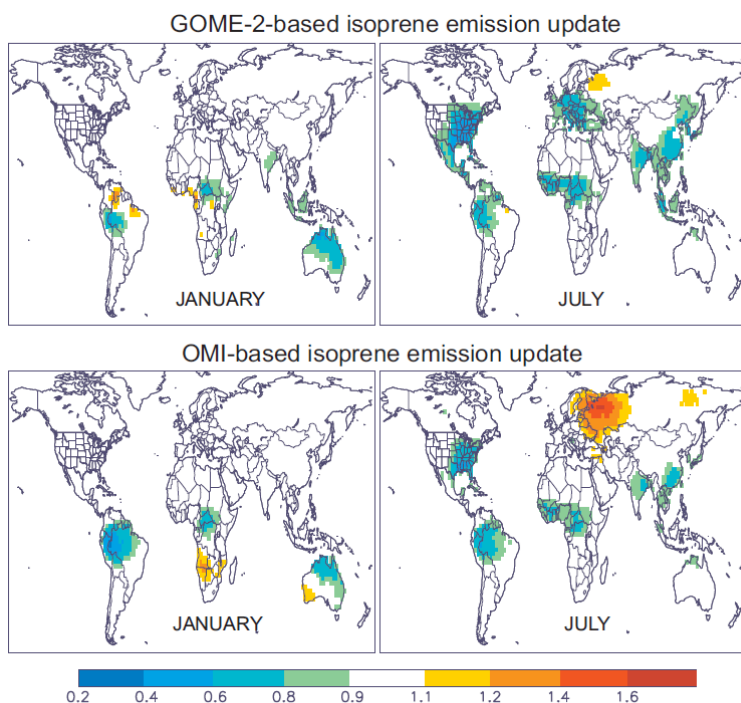


Figure 7. Ratios of optimized to a priori isoprene fluxes derived by source inversion of HCHO columns from GOME-2 (upper panels) and OMI (lower panels) in January and July 2010.

4.3 EVALUATION AGAINST GROUND-BASED MEASUREMENTS

Figure 8 illustrates a comparison between a priori and updated isoprene fluxes with ground-based flux measurements from 15 field campaigns in the Amazon. The flux measurements vary between 0.26 and 3.35 mg/m²/h depending on the season and the year of the measurement. The comparison accounts for the diurnal variations in the fluxes through correction factors used to scale the measured fluxes to daily averages. Direct comparisons between modelled fluxes and field measurements should, however, be carried out with caution mainly due to the coarse resolution of the modelled fluxes and of the satellite data used as top-down constraints, but also to the fact that flux measurements were often performed outside the study period (2005-2013), so direct comparison was not possible. The observed isoprene fluxes exhibit strong local differences within the forest (up to 5 mg/m²/h, [RD-Karl2007]) as well as significant differences from one day to another (up to 0.5 mg/m²/h, [RD-Ciccioli2003; RD-Karl2007; RD-Kuhn2007]), whereas they might exhibit differences of up to 1 mg/m²/h associated with the use of different measurement techniques [RD-Helmig1998; RD-Karl2007; RD-Kuhn2007].

Overall the emission reduction proposed based on the satellite observations lies within the variability of the field measurements. Note however, that the discrepancies between the observed ground based fluxes are often larger than the differences between the a priori and a posteriori fluxes. The field studies generally agree on higher fluxes during the dry and the dry-to-wet transition season between July and December [RD-Simon2005], while a recent field campaign suggests much lower fluxes (by ca. factor of 3) compared to the top-down estimates, most likely related to a local effect of leaf flushing at this location [RD-Alves2015].

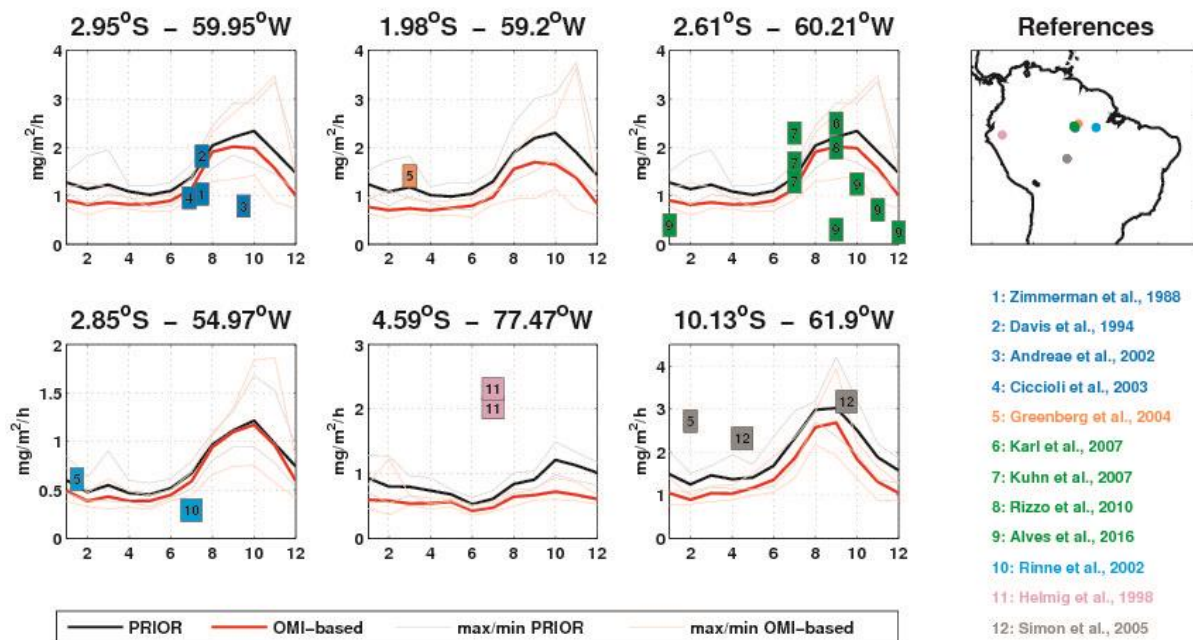


Figure 8. Comparison between a priori (black) and satellite based (red) isoprene fluxes to ground-based flux measurements (colored numbered squares). The a priori and a posteriori isoprene fluxes are averaged over the full period from 2005 to 2013 for the grid on which the ground site is located. To ensure meaningful comparison, the flux measurements are corrected for the diurnal variation in isoprene fluxes.

5. ANTHROPOGENIC VOC EMISSIONS OVER ASIA (BIRA-IASB)

5.1 EVALUATION AGAINST EMISSION INVENTORIES

The dominant emission source in China is anthropogenic and is estimated to lie between 15.6 TgVOC for 2005 [RD-Bo2008] and 27.1 TgVOC for 2008 (REASv2, [RD-Kurokawa2013]). The OMI-based inversion yields slightly higher estimates compared with REASv2 (Figure 9). The top-down estimates remain overall close to the REASv2 inventory that is used as a priori, but the emission patterns are modified, as illustrated in Figure 9. In northeastern China and in particular in the Beijing region, the emissions are increased by 20–40 %, whereas a reduction is inferred in the southeastern part of the country in particular around Shanghai (15–47%) and Guangzhou (15–30%). The flux distributions from the GOME-2-based inversion has common features, e.g., decreased fluxes in Shanghai and Guangzhou regions, but contradicting estimates in the northeast where GOME-2 observations do not support the emission enhancements suggested by OMI [RD-Stavrou2015]. The top-down fluxes are higher than all previously reported estimates for China. The satellite observations of HCHO suggest 2008 as the peak emission year, followed by strongly reduced fluxes in 2009 and 2010, and stabilized fluxes after that year.

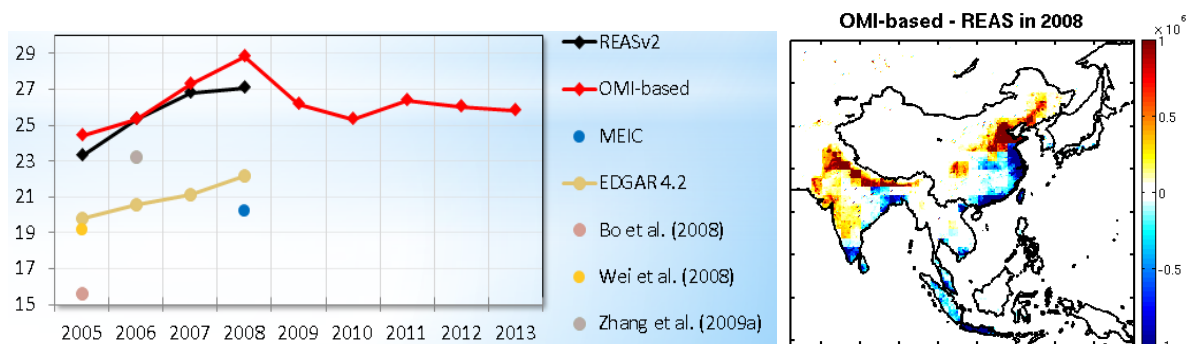


Figure 9. Left : Annual anthropogenic VOC emissions over China according to different emission inventories. Right : absolute difference between OMI-based and a priori REASv2 VOC (units are in kg/grid/year).

5.2 EVALUATION AGAINST SATELLITE OBSERVATIONS

We use GOME-2 HCHO columns as top-down constraints in an inversion conducted for year 2010. The global anthropogenic source is decreased in the GOME-2 inversion, while it is slightly increased in the inversion using OMI. Despite their limited capability to constrain this emission category on the global scale due to the small contribution of anthropogenic VOC emissions to the global HCHO budget [RD-Stavrakou2009], the satellite observations are found to provide constraints over highly polluted regions, notably in eastern China (Figure 10).

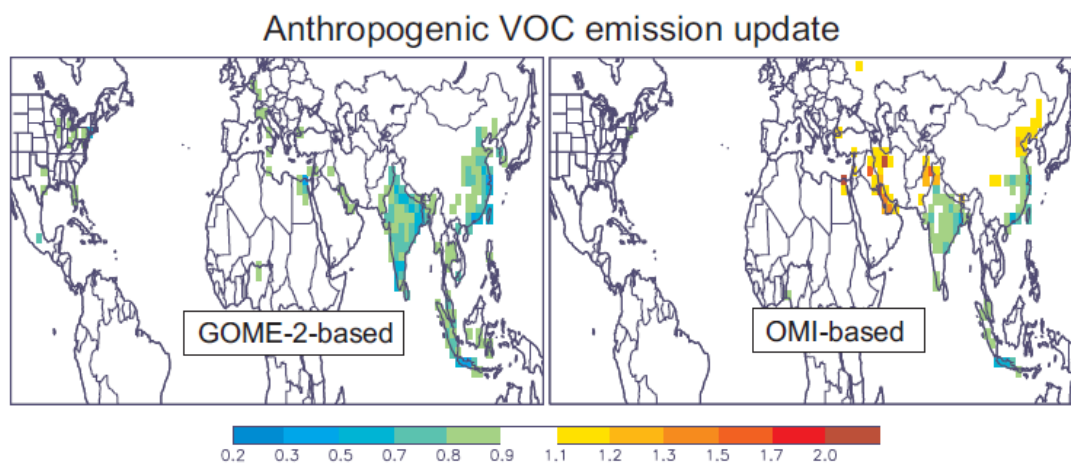


Figure 10. Ratios of optimized to a priori annual anthropogenic VOC fluxes derived by source inversion of HCHO columns from GOME-2 and OMI.

5.3 EVALUATION AGAINST GROUND-BASED MEASUREMENTS

In IMAGES model, to evaluate the diurnal cycle of the modeled HCHO column, we use ground-based, remotely sensed measurements at the following sites [RD-Stavrou2015] :

1. Uccle, Belgium (50.78 N, 4.35 E),
1 May 2011– 23 April 2012 [RD-Gielen2014].
2. Beijing, China (39.98 N, 116.38 E),
3 July 2008– 17 April 2009 [RD-Hendrick2014; RD-Vlemmix2015].
3. Xianghe, China (39.75 N, 116.96 E),
7 March 2010– 26 December 2009 [RD-Hendrick2014; RD-Vlemmix2015].
4. Bujumbura, Burundi (3 S, 29 E),
25 November 2013– 22 January 2014 [RD-DeSmedt2015].
5. Reunion Island, France (20.9 S, 55.5 E),
1 August 2004–25 October 2004, 21 May 2007–15 October 2007, 2 June 2009–28 December 2009, and 11 January 2010– 16 December 2010 [RD-Vigouroux2009].

The MAX-DOAS (Multi-axis differential optical absorption spectroscopy) technique [RD-Hönninger2004; RD-Platt2008] was used in all cases, except at Reunion Island where the FTIR (Fourier transform infrared spectroscopy) technique is used [RD-Griffiths2007; RD-Vigouroux2009]. Total HCHO columns are measured at all stations, and profiles are also measured at Beijing, Xianghe, and Bujumbura. Figure 11 illustrates the diurnal cycle of observed and modeled HCHO columns seasonally averaged and normalized by their noon values. The ratio of the observed columns at 13:30 and 09:30 LT ranges mostly between 0.8 and 1.2. The modeled values of this ratio are most often higher than in the measurements. The average ratio at all sites and seasons is slightly higher in the model (1.126) than in the data (1.043), although the average absolute deviation between model and data is large (20 %), presumably mostly because of representativity issues. The coarse resolution of the model makes it impossible to reproduce the very large differences seen, for example, between the observed diurnal profiles at Beijing and Xianghe, two sites very near to each other and within the same model grid cell. Nevertheless, the diurnal cycle of HCHO columns at the most polluted sites (Uccle, Beijing and Xianghe) shows a consistent pattern during summertime (also in spring and fall at Uccle) which is well reproduced by the model. Additionally, at Reunion Island, the observed midday maximum is well reproduced by the model. As pointed out above, the midday maximum at both very remote and very polluted sites is primarily caused by the diurnal cycle of OH levels, as the reaction with OH of the (mostly fairly long-lived) anthropogenic VOCs as well as methane is the main source of HCHO in those areas. In the Beijing area, the diurnal cycle of emissions is responsible for a slight delay in the maximum towards the afternoon, in agreement with the observations. A broader network of measurements would be necessary to provide a more detailed assessment of HCHO column diurnal variations, in particular over forests and in biomass burning areas. Nevertheless, the comparison presented here with the limited data set of available measurements revealed no large systematic discrepancies, except for a slight overestimation (by 8 %) of the average ratio of 13:30 to 09:30 LT columns.

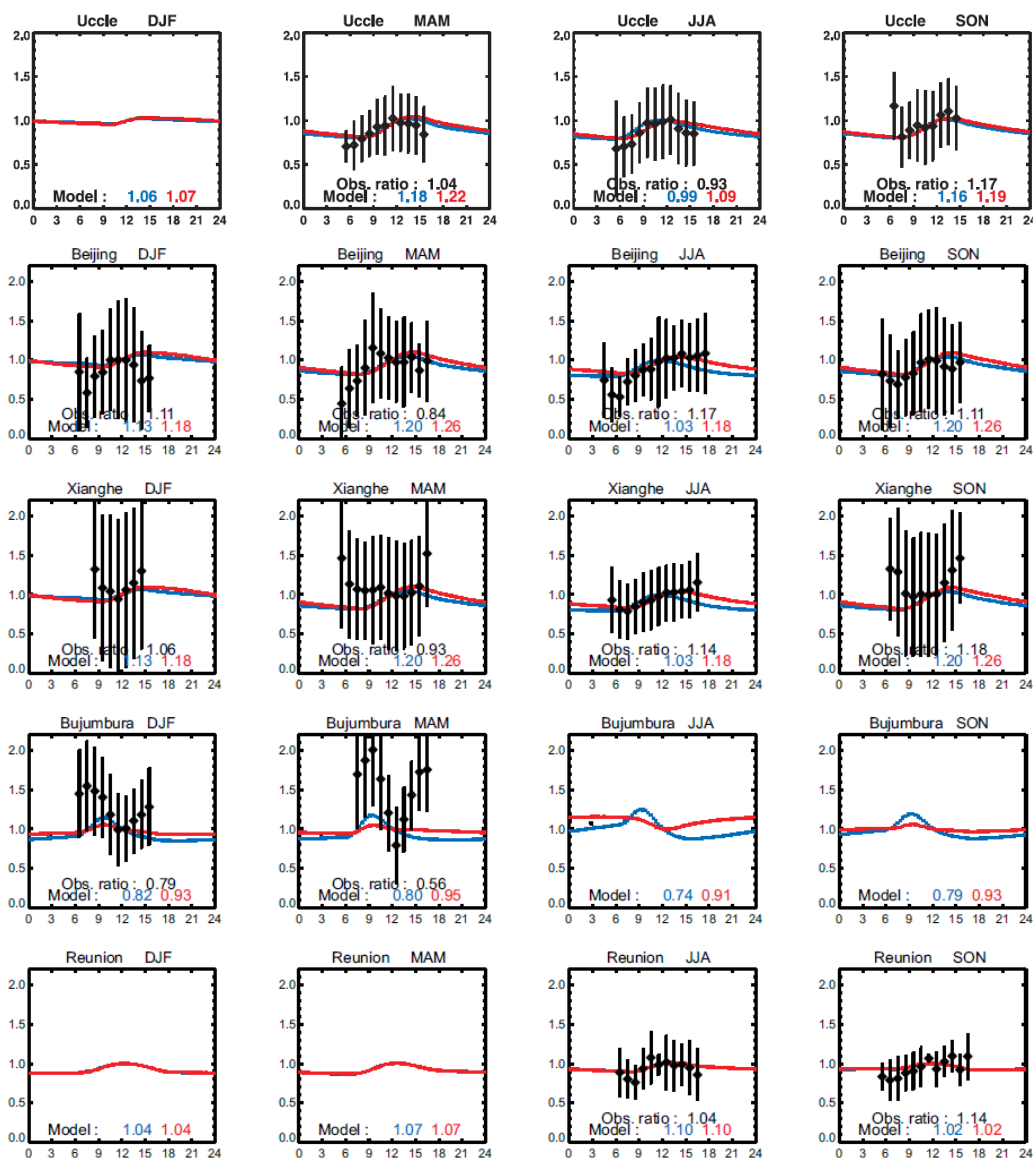


Figure 11. Seasonally averaged observed (black) and modeled (red) diurnal variations of HCHO columns normalized at noon at Uccle, Beijing, Xianghe, Bujumbura and Reunion Island. The observed columns are obtained using the MAX-DOAS and FTIR (Reunion Island) techniques. The error bars correspond to the measurement standard deviation. Modeled columns calculated assuming no diurnal emission variability are shown in blue. The observed and modeled ratios (blue and red) of 13:30 to 09:30 LT columns are given inset.

6. NOX EMISSIONS AND TRENDS IN EUROPE (TNO)

6.1 EVALUATION AGAINST SATELLITE OBSERVATIONS

We evaluate the discrepancies in the anthropogenic NO_x emission trends across Europe derived from OMI and GOME-2 datasets and the LOTOS-EUROS chemistry transport model. The chemistry transport model captures a large fraction of the variability in NO₂ columns at a synoptic timescale, although a seasonal signal in the bias between the modelled and retrieved column data remains. We make use of the Royal Netherlands Meteorological Institute (KNMI) OMI (DOMINO2 v2.0) and GOME-2 (TM4NO2A v2.3) tropospheric NO₂ vertical column density (VCD). Spatial patterns between GOME-2 and OMI for the multi-year averages are highly consistent over the entire domain of interest. However, quantitative comparison between the products indicates the GOME-2 VCDs are significantly higher than OMI VCDs. The bias between datasets presents an horizontal spatial gradient with a decrease in bias with the NO₂ vertical column density. The higher GOME-2 VCD values might reflect a longer chemical lifetime of NO_x in midmorning than the OMI observation time of early afternoon. The substantial difference between the two datasets raises an obvious question of consistency in potential science applications to estimate emission strengths. Though trends might be similar. However, between 2007 and 2013 the trends derived from GOME-2 and OMI have a similar distribution across Europe. The detection of a significant trends across Europe is scarce. Over North Western Europe no significant trends could be retrieved from either GOME-2 or OMI dataset. Over other area across Europe the amplitude in the trends derived from OMI and the trends derived from GOME-2 cannot be reconciled. In practice, across Eastern Europe a positive trends up to 30% is observed in OMI dataset while a positive trends up to 5% is present in GOME-2 datasets.

The aggregated trend in NO_x, derived by used of satellite retrieved NO₂ tropospheric columns and the chemistry transport model LOTOS-EUROS during 2007-2013 across Europe, is evaluated against measurements obtained from the AIRBASE network. A comparative study on in-situ NO₂ measurements shows annual reductions at the surface is of 1-3 %a⁻¹ for country in Western Europe. However, a significant number of station across Europe present annual increase in-situ NO₂ measurements at the surface.

Figure 12 to **Error! Reference source not found.**14 show the trends in NO_x for 2007-2013 per European country derived from AIRBASE, OMI and GOME-2 datasets, respectively. For most countries the amplitude of the trends is not straightforward. The boxplots distribution show that the various datasets agree in the trends sign for most of the countries across Europe. Additionally, the median trends seems to be similar for several countries. For western and northern European countries the sign of the median trends agrees for most stations. However, the amplitude and the spread of trends from AIRBASE, OMI and GOME-2 datasets cannot be reconciled.

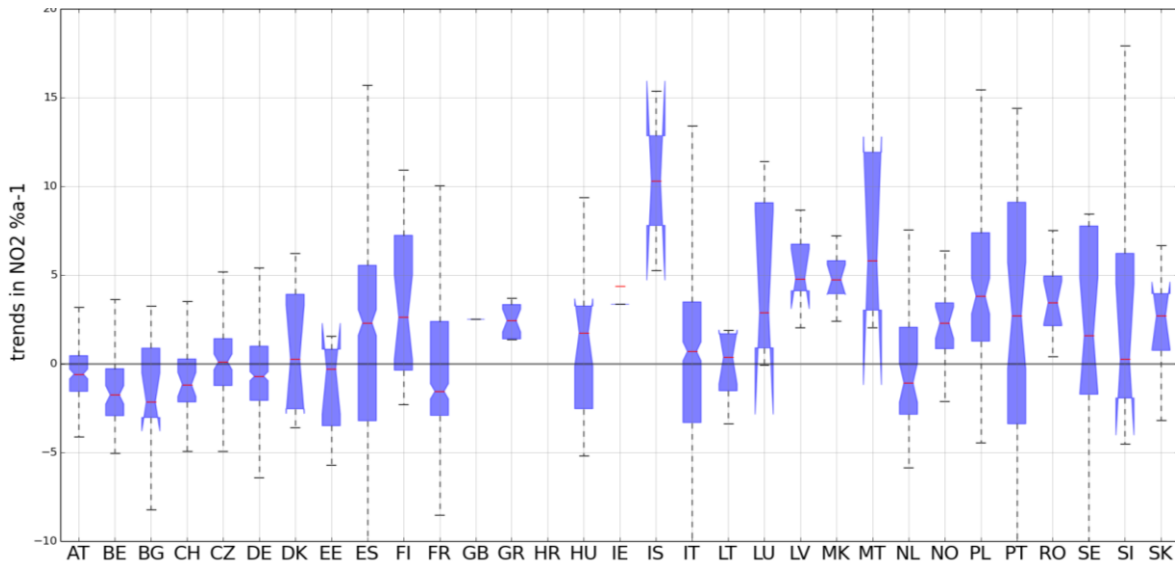


Figure 12. Trends in NO_x for 2007-2013 per European country derived from AIRBASE datasets

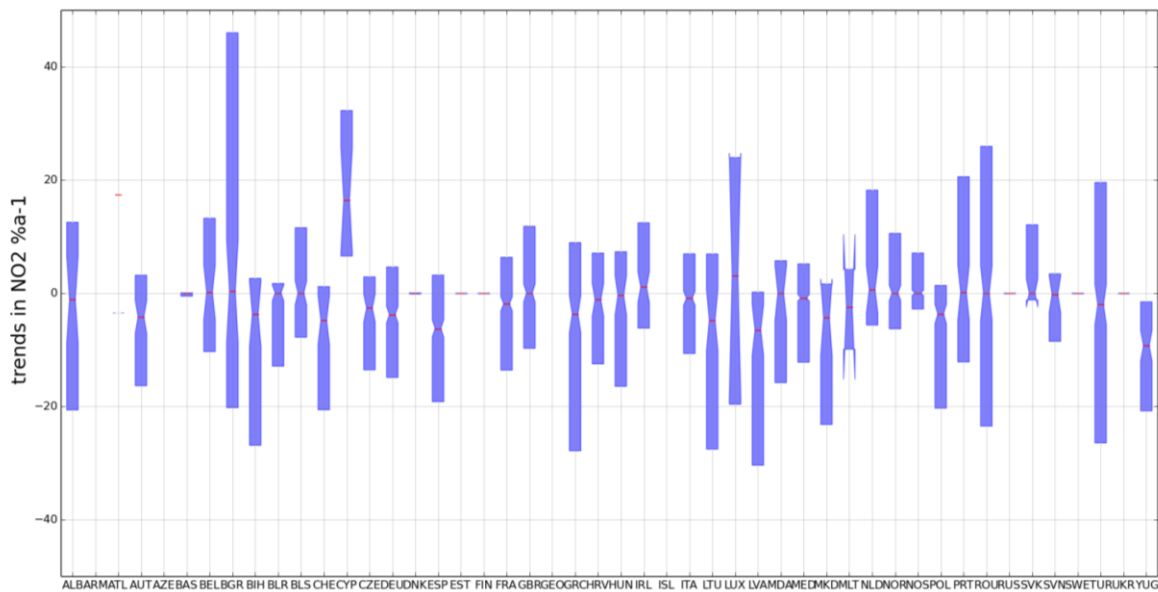


Figure 23. As previous for OMI.

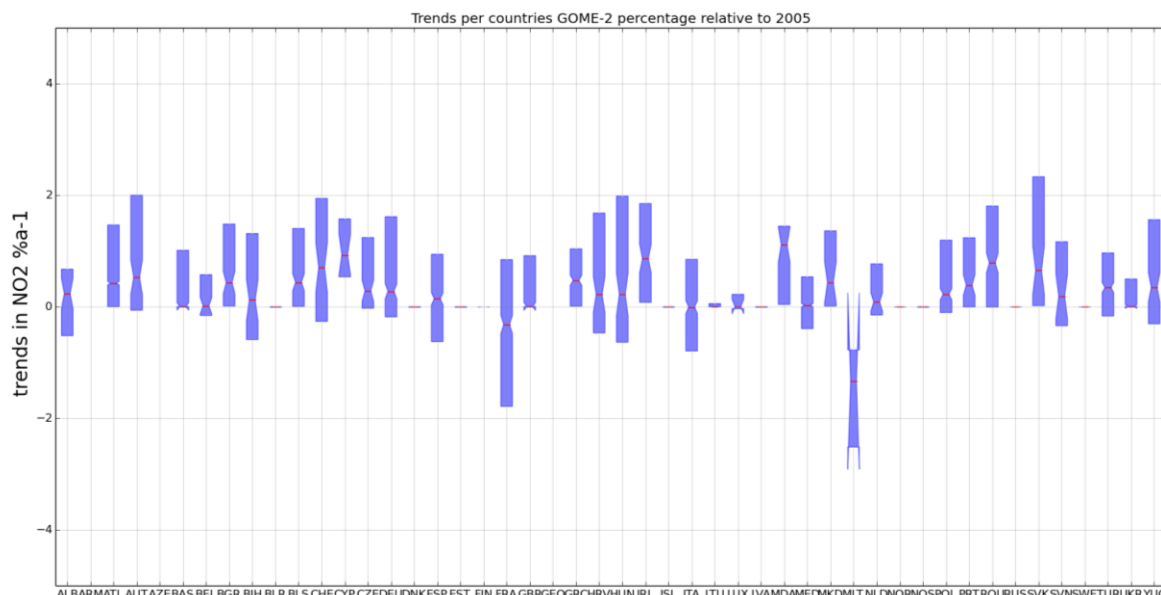


Figure 34. As previous for GOME-2.

6.2 EVALUATION AGAINST GROUND-BASED MEASUREMENTS

The evaluation of the tropospheric NO₂ column modelled by LOTOS-EUROS has been combined with MACC-Val activity. The LOTOS-EUROS tropospheric NO₂ column were part of a multi-model comparisons [RD-Blechtschmidt2015]. For this comparison study, tropospheric NO₂ columns from MAX-DOAS instruments at three different European stations were compared to results from five regional air quality models (LOTOS-EUROS, CHIMERE, EMEP, MOCAGE and SILAM). The study concluded that the agreement between model and measurements was good for the majority of measurements with an overall correlation of about 60 % and 40 % for NO₂ VCDs and surface partial columns, respectively. The ability of the models to reproduce the measurements shows quite a large day-to-day variability. Whereas weekly cycles are simulated rather well by the models, there is strong disagreement between measurements and simulations for seasonal and especially diurnal cycles. On average, wind directional distributions of NO₂ are well reproduced by the models. As the sensitivity of MAX-DOAS retrievals is largest in the boundary layer, we initially expected the application of averaging kernels from the measurements to model simulations to be of crucial importance for validation results. Surprisingly, it was shown that in case of MAX-DOAS retrieval the averaging kernels on the data analysis had a negligible impact. However, this can be explained by the fact that both models and measurements show the largest NO₂ partial columns close to the surface. A more in depth evaluation of the results can be found in "MAX-DOAS tropospheric NO₂ column retrievals as a validation tool for regional air quality models of the upcoming Copernicus Atmosphere Monitoring Service" [RD-Blechtschmidt2015].

7. REGIONAL NO_x EMISSION INVENTORIES (KNMI)

7.1 THE DECSO EMISSION ESTIMATION ALGORITHM OVERVIEW

The DECSO algorithm [RD-Mijling2012] is specifically designed to use daily satellite observations of column concentrations for fast updates of emission estimates of short-lived atmospheric constituents on a mesoscopic scale (0.25°×0.25°). An extensive description of the algorithm can be found in the GlobEmission ATBD [RD-ATBDv3].

We use the DECSO algorithm together with the regional CTM CHIMERE [RD-Schmidt2001; RD-Bessagnet2014] on a 0.25° resolution, driven by operational meteorological forecast of the European Centre for Medium-Range Weather Forecasts (ECWMF). The CTM implementation is described in more detail by [RD-Mijling2009]. We use NO₂ observations from the OMI or the GOME-2 instrument. From 1 January 2013 onward, the DECSO-v3a series for GOME-2 are based on GOME-2B retrievals. Tropospheric NO₂ column retrievals are calculated with the DOMINO v2 algorithm [RD-Boersma2011] from spectral measurements between 426–451 nm. Cloud fraction and cloud height are derived from the oxygen-A band [RD-Koelemeijer2001]. NO₂ retrievals at cloud fractions larger than 20% are filtered out to reduce the influence of the modelled NO₂ column below the clouds. Retrievals with low clouds (below 800 hPa) are also rejected because the intersection of the cloud with the NO_x bulk makes the retrieval too sensitive for the exact cloud height. Before comparing the model simulations with the satellite observations, the CHIMERE vertical profiles are extended from the model ceiling (at 500 hPa) to the tropopause with a climatological partial column. The profiles are then interpolated to the observational footprints (having a lower spatial resolution), after which the averaging kernel can be directly applied, see [RD-Mijling2012].

Table 4. Overview of the available regional NO_x emission inventories

Domain	Range	Algorithm version	Instrument	Initial emission inventory	Period
East China	18°N - 50°N, 102°E - 132°E	DECSO-v3a	OMI	MEIC (January 2008)	2007-2014 (monthly)
			GOME-2	MEIC (January 2008)	2007-2014 (monthly)
Middle East	20.25°N - 37.75°N, 29.5°E - 63.25°E	DECSO-v3a	OMI	EDGAR v4.2 (2008)	2010-2011 (monthly)
		DECSO-v3b	OMI	HTAPv2/ EDGAR v4.3 (2010)	2007-2014 (monthly)
South Africa	9°S - 37°S, 10°E - 42°E	DECSO-v2	OMI	EDGAR v4.2 (2008)	2009-2010 (monthly)

India	4°N - 34°N, 67°E - 92°E	DECSO-v2	OMI	EDGAR v4.2 (2008)	2007-2008 (monthly)
-------	----------------------------	----------	-----	-------------------	------------------------

DECSO version improvements from v2 to v3a mainly consider optimisation of the calculation speed of the concentration-to-emission sensitivities and the inversion by the Kalman filter. In DECSO version v3b, the CTM CHIMERE V200606A was replaced by the more recent CHIMERE v2013b. Also, the land use database was updated from GLCF 1993 to GlobCover 2009. A better outlier analysis was implemented to suppress unrealistic emission updates.

7.2 EVALUATION OF EAST ASIAN EMISSIONS AGAINST EXISTING INVENTORIES

The GlobEmission NO_x emission inventory covers East Asia from 18°N to 50°N and 102°E to 132°E on a 0.25° resolution. Apart from the populated and industrialized provinces of East China, the domain contains North and South Korea, Japanese Kyushu Island, and significant parts of Mongolia and Vietnam.

7.2.1 MEIC inventory

The emission results of 2008 are compared with the Multi-resolution Emission Inventory for China (MEIC) [RD-He2012] for 2008 regridded to the DECSO emission grid, see Figure 15 and 16. Outside China, where no MEIC emissions are defined, the emission inventory is compared with the INTEX-B inventory [RD-Zhang 2009].

The satellite derived emissions reveal ship tracks along the Chinese south and west coast, and shipping emissions in the heavily navigated Bohai sea. They also improve the resolution of the INTEX-B emission inventory (0.5 degree) used outside China.

Compared to MEIC 2008, the NO_x emission totals for East China are about 22% lower than the MEIC estimates for East China in 2008 (7.53 Tg N/yr, Table 5). Several hot spots, such as emissions from power plants in northeast China, appear to be underestimated with respect to MEIC 2008. On the other side, also new hot spots are detected which are unaccounted for in the bottom-up inventory. The inversion method introduces a positively biased emission noise in remote areas, such as unnavigated areas in the East China Sea. This bias might also affect Mongolia, although it is shown in [RD-Mijling2013], that the seasonal cycle on the retrieved emissions in this country correspond to the expected biogenic soil emissions due to the rainy season.

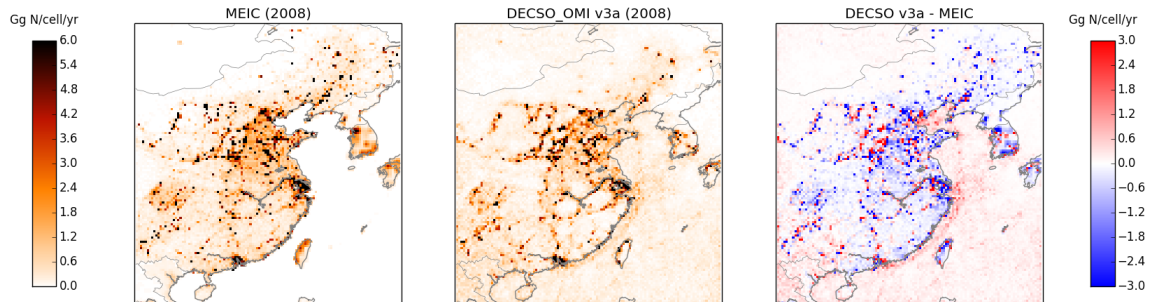


Figure 15. The total anthropogenic NO_x emission inventory from MEIC for 2008 compared with the DECSO –OMI v3a inventory for the same year.

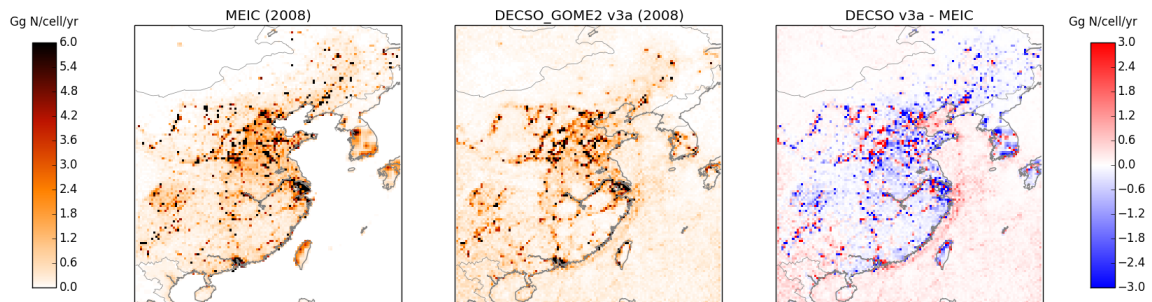


Figure 16. The total anthropogenic NO_x emission inventory from MEIC for 2008 compared with the DECSO –GOME2 v3a inventory for the same year.

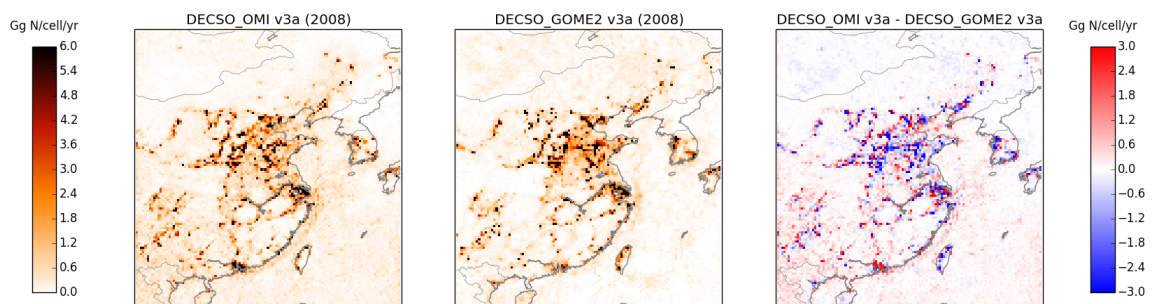


Figure 17. Comparison of the DECSO v3a NO_x emission inventories derived from OMI and GOME-2 measurements.

The intercomparison of the emission inventories for 2008 derived from OMI measurements and GOME-2 measurements (Figure 17) shows the dependency of the emission estimation on the satellite instrument. Most local differences can be attributed to the difference in spatial resolution between OMI (24x13 km² in nadir, to 68x14 km² at edges) and GOME-2 (80x40 km² in nadir, to 90x65 km² at edges). The coarser resolution of the GOME-2 instrument troubles the

determination of the exact location of the emissions on the 0.25 degree grid. As can be seen from Table 5, both instruments agree within 5% on the total NO_x emissions in East China.

Table 5. MEIC emissions totals compared to DECSOv3a [Tg N/yr]

	MEIC		DECSO-OMI v3a								DECSO-GOME2 v3a							
	2008	2010	2007	2008	2009	2010	2011	2012	2013	2014	2007	2008	2009	2010	2011	2012	2013	2014
East China	7.534	8.279	5.826	5.704	5.724	6.605	7.395	7.618	7.442	7.151	5.951	5.989	5.839	6.893	7.446	7.581	7.108	6.534
Land	7.535	8.280	6.498	6.427	6.386	7.264	8.168	8.445	8.299	8.112	6.622	6.689	6.530	7.523	8.116	8.330	7.801	7.311
Land + Sea	7.594	8.339	7.314	7.429	7.436	8.338	9.351	9.746	9.715	9.822	7.025	7.119	6.957	7.954	8.557	9.036	8.413	7.982

Figures 18 and 19 show the yearly NO_x emission trends for Chinese provinces based on OMI and GOME-2 observations. In Beijing, where strict emission are quality policies are enforced to control the air quality in the growing city, the NO_x emissions peak in 2010. Other provinces show later emission peak years, while emissions for provinces like Jiangxi continue growing.

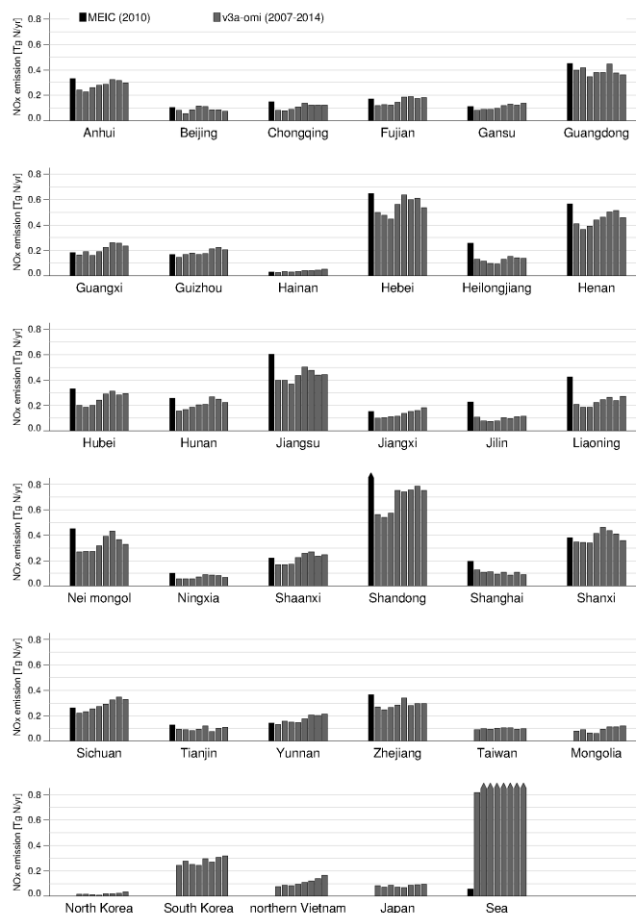


Figure 18. MEIC emissions compared to DECSO-OMI v3a emissions by Chinese province. Note that some provinces are only partly included in the emission

domain: Gansu (61%), Heilongjiang (74%), Nei Mongolia (83%), Sichuan (51%), Yunnan (36%).

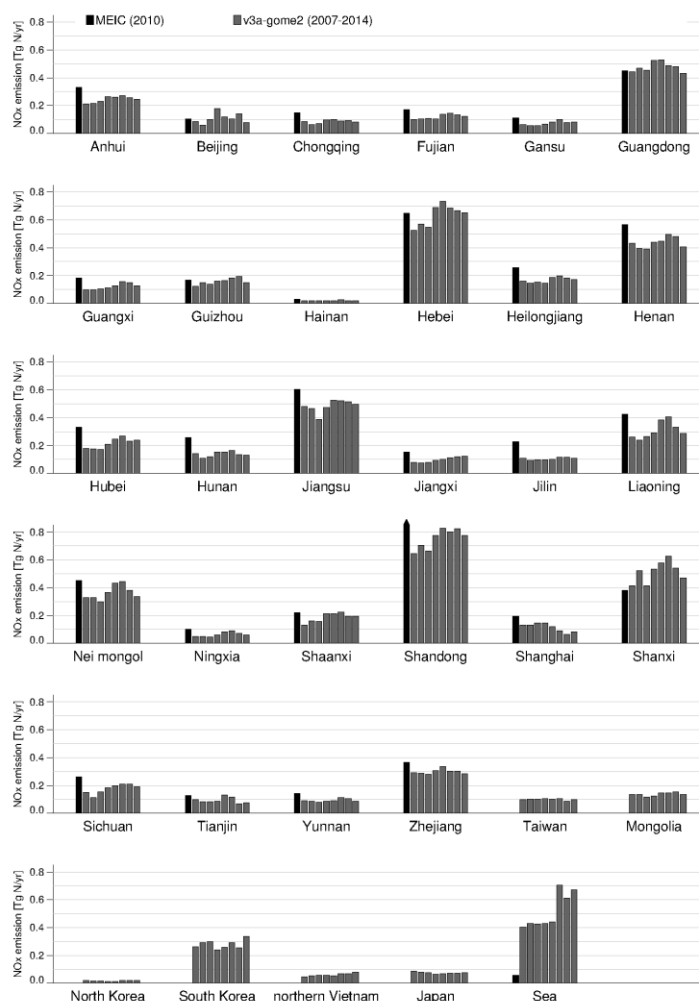


Figure 19. MEIC emissions compared to DECSO-GOME2 v3a emissions by Chinese province

7. 2.2 South Korean CAPPS inventory

The DECSO emission inventories for South Korea have been compared by prof. SeogYeon Cho, from INHA university. The left panel in Figure 20 shows that the total national emissions compare relatively well. The DECSO emissions are generally lower, although this is partly due to a more stringent region definition (i.e. neglecting sea). The comparison is based on the old algorithm version DECSOv1 (as was published in the first phase of GlobEmission). The right panel of Figure 20 shows how values change when switching to DECSOv3a. For both GOME-2 and OMI, yearly totals increase, and show better correspondence with the CAPPS bottom-up values. All satellite-derived products show an emission minimum for 2010.

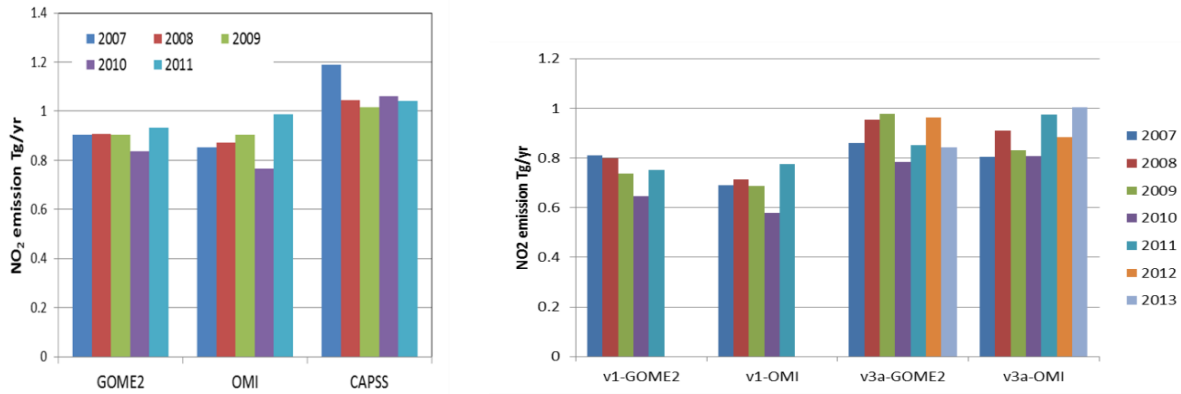


Figure 20. Comparison of NO_x emissions for South Korea with the CAPPS emission inventory

7.3 EVALUATION OF MIDDLE EAST EMISSIONS AGAINST EXISTING INVENTORIES

The GlobEmission NO_x emission inventory covers the Middle East from 20.25°N to 37.75°N and 29.5°E to 63.25°E on a 0.25° resolution. It contains the entire Persian Gulf, with a relative central location of Qatar. It also contains Saudi Arabia and large part of Iran, Eastern Mediterranean countries, Cairo and the Nile river, and the shipping routes in the Red Sea and the Persian Gulf.

One of the few gridded emission inventories available for the Middle East is the global EDGAR inventory. The latest version, EDGAR v4.3, is part from the HTAP v2 data set [RD-JRC2015]: 0.1 degree gridded maps of CH₄, CO, SO₂, NO_x, NMVOC, NH₃, PM₁₀, PM_{2.5}, BC and OC for the years 2008 and 2010. As opposed to the previous version v4.2 [RD-EDGAR2009], it contains shipping emissions.

EDGAR v4.2 was used as an initial inventory for the DECSO_OMI v3a dataset. As can be seen in Figure 21, EDGAR v4.2 contains unrealistic features in NO_x emissions, such as strong emission lines along the borders of United Arab Emirates and Kuwait. These features disappear in the inversion. The DECSO results also show ship tracks in the Red Sea and the Gulf of Aden, and strong emissions in the Persian Gulf, due to shipping and offshore oil and gas industry. Unknown sources, such as emissions related to oil production in Yemen are also discovered.

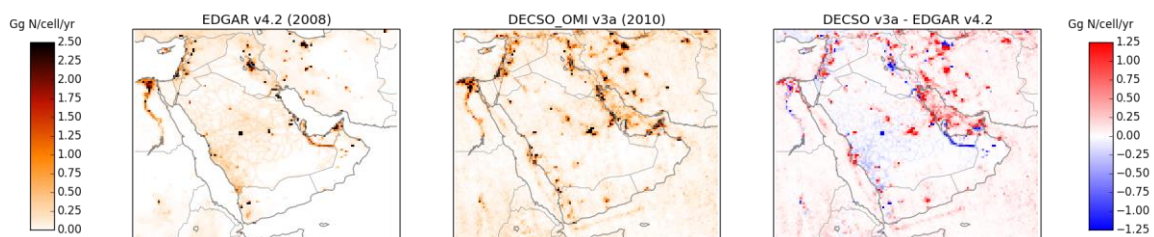


Figure 21. The total anthropogenic NO_x emission inventory from EDGAR v4.2 for 2008 compared with the DECSO-OMI v3a inventory for 2010.

Improved results are obtained with the newer version DECSO v3b (see Figure 22). Striking feature are the changed ship tracks taken since 2009 in the Gulf of Aden to avoid pirate attacks from Somalia. Before the coast of Oman, the shipping routes become too disperse to be detected.

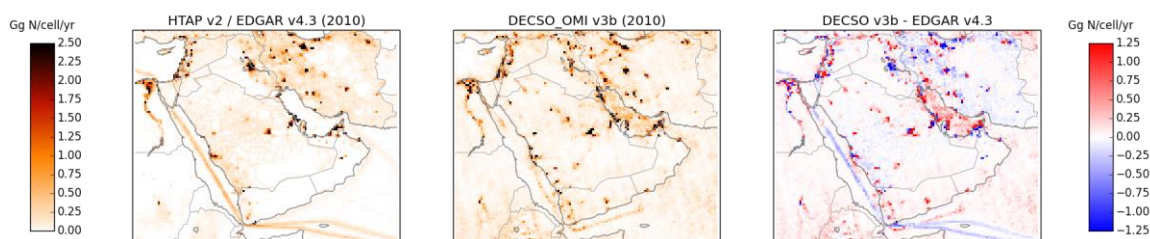


Figure 22. The total anthropogenic NO_x emission inventory from EDGAR v4.3 for 2010 compared with the DECSO-OMI v3b inventory for the same year.

Country totals of NO_x emissions are listed in Table 61. Note that for countries which are not fully included in the emission inventory domain, the emissions do not reflect the national total. Also note that part of the emission increases during 2007-2014 is not real, but due to the OMI row anomaly (<http://www.temis.nl/airpollution/no2col/warning.html>) and pixel-to-pixel biases. In future processings, the OMI observations for this region will be better filtered and de-stripped.

Table 6. EDGARv4.3 emissions compared to DECSOv3b emissions for Middle Eastern countries [Gg N/yr]

	EDGAR v4.3	DECSO-OMI v3b							
	2010	2007	2008	2009	2010	2011	2012	2013	2014
Afghanistan	4.5	9.4	8.1	8.1	13.1	17.1	24.2	18.7	21.8
U.A.E.	90.9	85.9	103.8	101.2	102.2	95.1	95.7	102.0	108.3
Bahrain	6.4	11.9	16.8	12.0	14.4	9.8	12.5	14.6	15.5
Cyprus	4.7	5.9	5.8	6.1	5.4	9.5	12.7	9.0	7.9
Iran	609.4	436.0	481.4	464.9	482.5	582.1	648.2	676.9	716.3
Iraq	214.5	122.1	155.6	168.0	164.1	233.2	261.7	292.4	290.4
Israel	42.9	40.1	42.4	38.0	32.2	39.6	44.2	40.6	38.4
Jordan	16.2	26.1	31.0	30.0	24.2	38.0	43.3	44.6	55.5
Kuwait	44.0	63.4	62.8	67.6	50.8	70.1	87.9	99.9	73.4
Lebanon	24.1	23.7	26.1	21.8	20.0	23.4	24.5	31.8	37.2
Oman	21.9	35.8	35.7	36.9	32.6	46.4	51.6	68.0	83.0
Djibouti	2.3	4.1	6.9	6.0	3.5	6.0	6.8	10.2	9.7
Egypt	138.4	176.3	191.3	181.5	176.3	228.4	243.7	246.0	283.2
Palestina	5.3	10.3	10.0	9.7	10.0	10.2	12.3	9.1	9.0
Qatar	26.8	31.5	42.6	40.7	33.1	47.1	46.7	46.5	55.6
Saudi Arabia	407.1	443.2	499.1	466.1	441.9	545.5	609.4	643.7	719.5
Syria	59.0	78.8	88.4	81.8	70.9	84.8	91.8	66.7	79.7
Turkmenistan	3.0	25.9	26.2	24.6	28.3	33.1	39.9	34.0	43.5
Turkey	42.5	58.0	72.7	59.1	54.8	70.4	88.7	90.3	102.6
Yemen	27.6	65.4	84.7	75.5	63.9	78.4	92.0	116.4	126.3
Pakistan	2.6	2.2	2.6	2.3	2.7	4.0	5.3	6.0	7.3
Somalia	0.9	10.2	17.1	13.6	11.8	16.7	26.5	40.3	40.7

Eritrea	1.9	14.6	17.1	12.1	9.2	14.1	15.1	20.1	24.5
Sudan	23.3	133.3	156.9	120.0	91.7	156.3	151.0	198.9	250.1
Ethiopia	12.1	83.6	103.7	71.1	62.6	92.4	95.0	130.2	155.0

7.4 EVALUATION OF SOUTH AFRICAN EMISSIONS AGAINST EXISTING INVENTORIES

The GlobEmission NO_x emission inventory covers southern Africa from 9°S to 37°S and 10°E to 42°E on a 0.25° resolution. EDGAR v4.2 was used as an initial inventory (Figure 23).

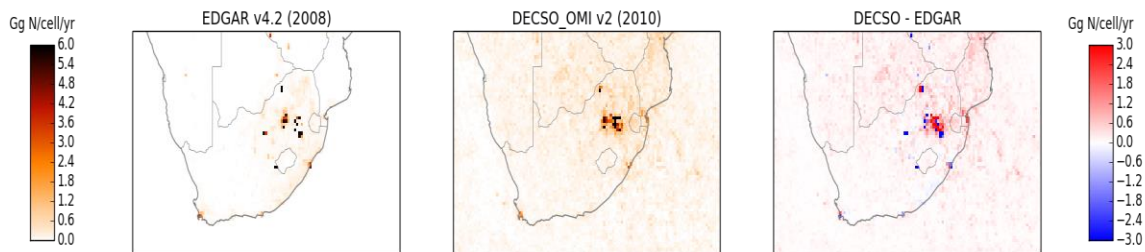


Figure 23. The total anthropogenic NO_x emission inventory from EDGAR v4.2 for 2008 compared with the DECSO–OMI v2 inventory for 2010.

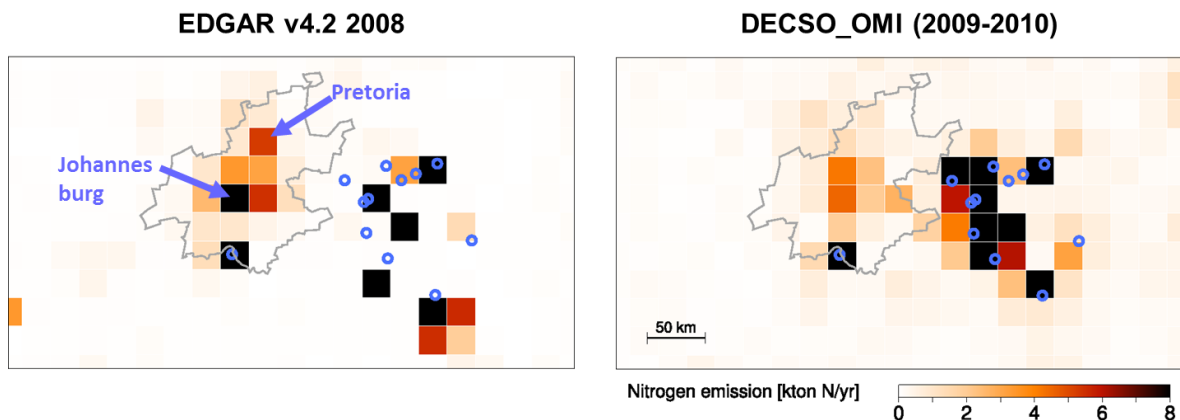


Figure 24. NO_x emissions for the South African Highveld. The blue circles indicate the location of coal-fired power stations.

Figure 24 shows the NO_x emissions for the South African Highveld. The grey outline indicate the densely populated Gauteng province, containing Johannesburg and Pretoria. The region to the east is home of several coal-fired power stations, important hot spots of NO_x emissions. The left panel shows the emission strength of the EDGAR v4.2 bottom-up emission inventory, based on 2008 data. The right panel shows the emission estimates from the OMI instrument for 2009–2010. Using satellite data improves the location of the emission hot spots.

7.5 EVALUATION OF INDIAN EMISSIONS AGAINST EXISTING INVENTORIES

The GlobEmission NO_x emission inventory covers the Indian subcontinent from 4°N to 34°N and 67°E to 92°E on a 0.25° resolution. Emission results over the Tibetan Plateau are masked due to the local breakdown of the inversion algorithm (mountain peaks sticking out of the CTM model ceiling).

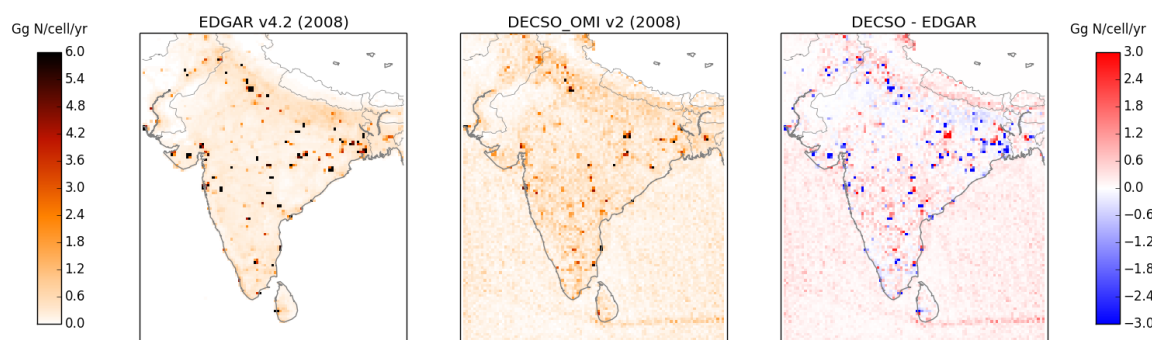
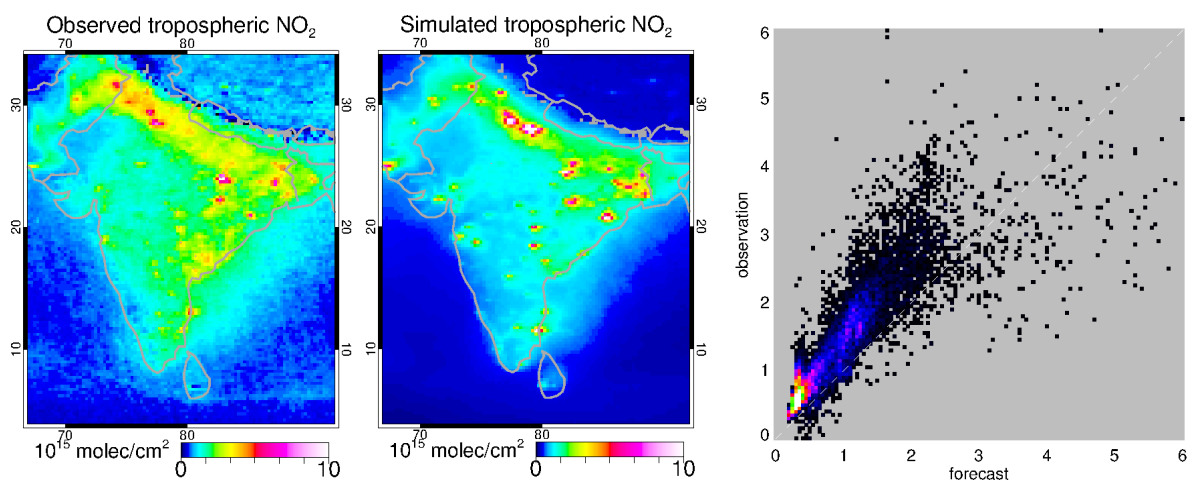


Figure 25. – The total anthropogenic NO_x emission inventory from EDGAR v4.2 for 2008 compared with the DECSO–OMI v2 inventory for the same year.

7.6 EVALUATION OF INDIAN EMISSIONS AGAINST SATELLITE OBSERVATIONS

As a consistency check, we run the CTM model for May–July 2008 with and without data assimilation of OMI observations. The upper middle panel in Figure 26 shows the collocated simulations of the free run, and the lower middle panel shows the simulation based on daily updated emissions. As can be seen by eye and in the scatter plots, the assimilation run results in average concentrations patterns which are better spatially correlated with the observations.



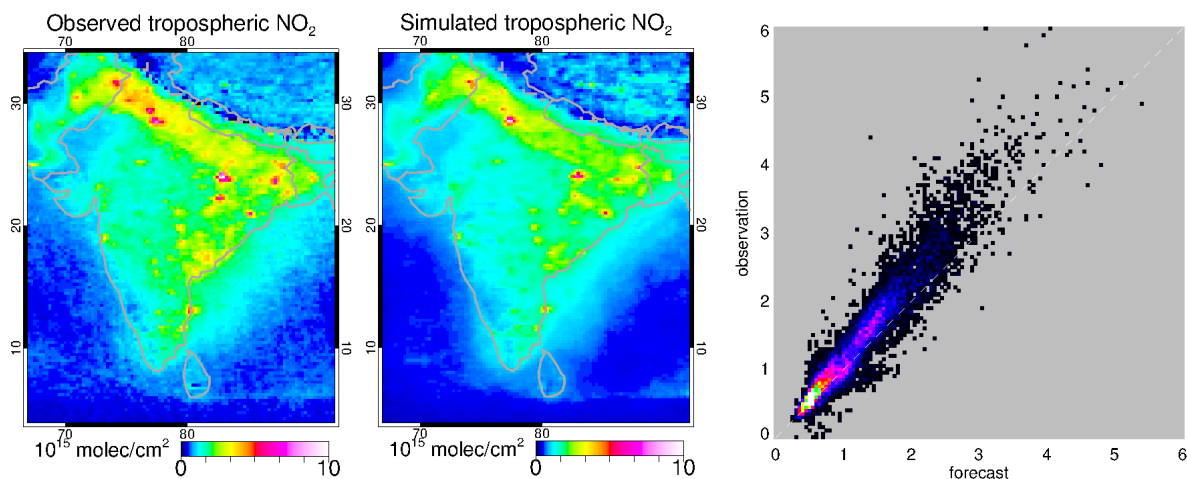


Figure 26. Simulation of tropospheric NO₂ columns by the CHIMERE model, without and with assimilation of the observations.

7.7 INVENTORY ISSUES, FUTURE IMPROVEMENTS

The DECSO algorithm for emission estimation is a relatively young algorithm, which is continuously being improved. As the emission estimates depend on unbiased satellite observations and model simulations and correct (non-local) relations between emissions and observations, errors can be attributed to satellite retrieval issues, CTM issues (including meteorology and chemistry), or invalid assumptions in the inverse calculation. The NO_x emission estimates as published in the current GlobEmission database, might suffer from the following issues, which will be addressed in future algorithm versions.

- Response time to emission changes. The algorithm uses daily satellite observations for a daily update of the emission inventory. The daily satellite observations do not cover the whole domain due to filtering of e.g. cloudy pixels, and are generally of a coarser resolution than the emission grid. This, together with large uncertainty in the satellite observation and the model simulation, would make a direct emission inversion mathematically ill-defined. The Kalman filter regulates this problem by using a priori information. This introduces a response time to emission changes which depends on the model and observation error, and the observation frequency in space and time. The time lag for seasonal variations in our current settings is estimated to be around a month [RD-Mijling 2013].
- Local dependency on satellite resolution. The DECSO algorithm gives consistent results for regional emissions totals when different satellite instruments are used. On a local scale, differences can occur related to the difference in spatial resolution between e.g. OMI (24x13 km² in nadir, to 68x14 km² at edges) and GOME-2 (80x40 km² in nadir, to 90x65 km² at edges). As a rule of thumb, the spatial resolution of the emission inventory corresponds to the spatial resolution of the satellite observations. However, due to

oversampling and accounting for non-local relations between observed concentration and emissions, the spatial resolution of the emission inventory will generally be higher.

- Emission noise. The DECSO algorithm updates emissions based on addition, and not by scaling existing emissions. This enables the algorithm to find new hot spots, and relocate existing hot spots. On the downside, as emissions cannot become negative, it can introduce a positively biased noise in low emitting areas, such as remote seas.
- Unrealistic seasonal cycles. The OMI-derived emissions show more unrealistic seasonal cycles than GOME-2. This is partly related to the late overpass time of the OMI instrument (13:30 local solar time, opposed to 9:30 for GOME-2), when photochemistry is more prominent. Large part comes from a cumulative effect of low values of seasonal dependent emission noise in low-emitting areas.

8. IS4FIRES INVENTORY (FMI)

The IS4FIRES products have been additionally evaluated against several criteria and datasets. The assessment and discussion on the related uncertainties has been published by [RD-Soares2015], in application to the AQMEII-II case study (Eurasian summer fires of 2010).

Removal of the non-fire sources from the MODIS fire database. Figure 2727 shows the outcome of masking out the highly energetic sources from MODIS-FRP database collection 5. There are clear cases of persistence of grid-cells that are reported as fires, in particular as areas such as Arabian Peninsula (Figure 27a). The impact of non-fire high-temperature sources in August of 2010 has been simulated with SILAM run with and without these sources (the difference is shown in Figure 27b) There is an impact when oil extraction/production plants in Russia are masked-out from the fire emission database. AOD can be reduced by ~80% in the immediate vicinity of these sources but the effect quickly falls out with distance from the oil flares.

Effect of modification of the land-use categorization. The IS4FIRES v.1 had two different land-uses: forest and grassland (plus a mixture of the two). This categorization has been reviewed and v.2 of the system includes 7 categories. Comparison with MODIS AOD observations shows that the single grassland category for the whole globe is sufficient (the evaluation results do not differ between the continents) but e.g. temperate forest has to be considered separately for each continent. This work, however, was postponed until v.2.1: increase of the land-use classes directly affects the well-posedness of the emission factor determination task. A more straightforward task was related to mis-attribution of some of the USGS land-use classes to the 7 selected categories. Being a minor issue at a global scale (Table 7 7), it strongly affects some individual cases. Assessment of the AOD histogram for each continent (Figure 288) showed substantial improvement of the system for Africa, where the over-estimation of the PM emission was suspected during the previous system evaluation. For Europe, the decent quality of already IS4FIRES v.1 is also seen: new recalibration resulted in limited improvements.

Summary and next steps. IS4FIRES v.2 validation efforts followed a series of improvements that allowed this system to provide substantially more accurate emission estimates, especially outside Europe. The on-going efforts concentrate on: (i) switch and evaluation of MODIS FRP collection 6 dataset, (ii) comparison with independent dataset of AATSR and in-situ data, (iii) application in various case studies and fire events, to collect more information of the data quality and their use practices by other modellers.

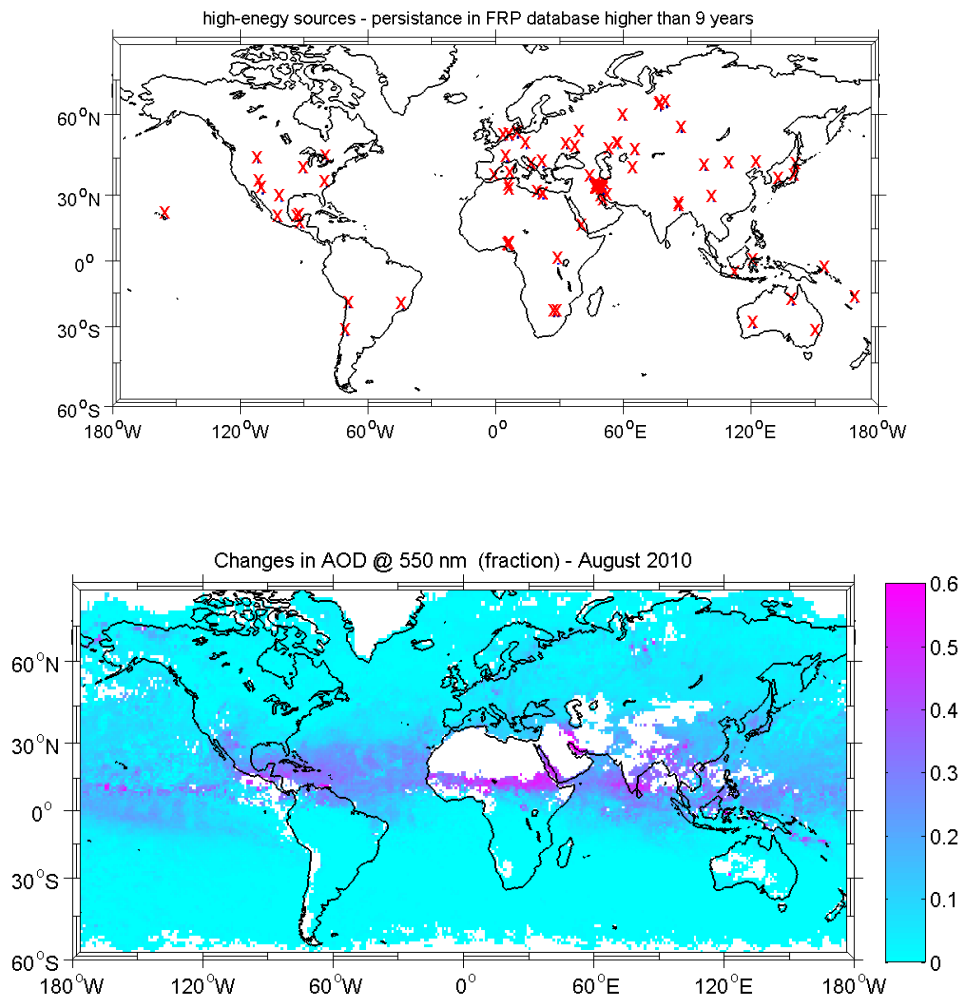


Figure 27. Upper panel: a map of non-fire pixels excluded from the MODIS database (red crosses); lower panel: relative AOD reduction due to masking out these pixels

Table 7. Statistics for the measured (MODIS) and predicted AOD (SILAM with IS4FIRESv1 (SILAM-IS4FIRESv1), with IS4FIRESv2 (SILAM-IS4FIRESv2), with IS4FIRESv2 with land-use classes redistributed to correct mis-attribution (SILAM-IS4FIRESv2nLU) for fire dominated cells (daily averages) for Eurasia and Africa: median, mean, root mean square (RMS), root mean square error (RMSE) and correlation coefficient (R).

		MODIS	SILAM IS4FIRESv1	SILAM IS4FIRESv2	SILAM IS4FIRESv2nLU
Eurasia	median	0.11	0.13	0.11	0.11
	mean	0.14	0.21	0.17	0.17
	RMS	0.17	0.35	0.27	0.27
	RMSE	-	0.27	0.19	0.19
	R	-	0.38	0.40	0.40
Africa	median	0.24	0.54	0.38	0.38
	mean	0.30	0.76	0.52	0.52
	RMS	0.36	1.01	0.67	0.67
	RMSE	-	0.69	0.37	0.37
	R	-	0.79	0.75	0.75

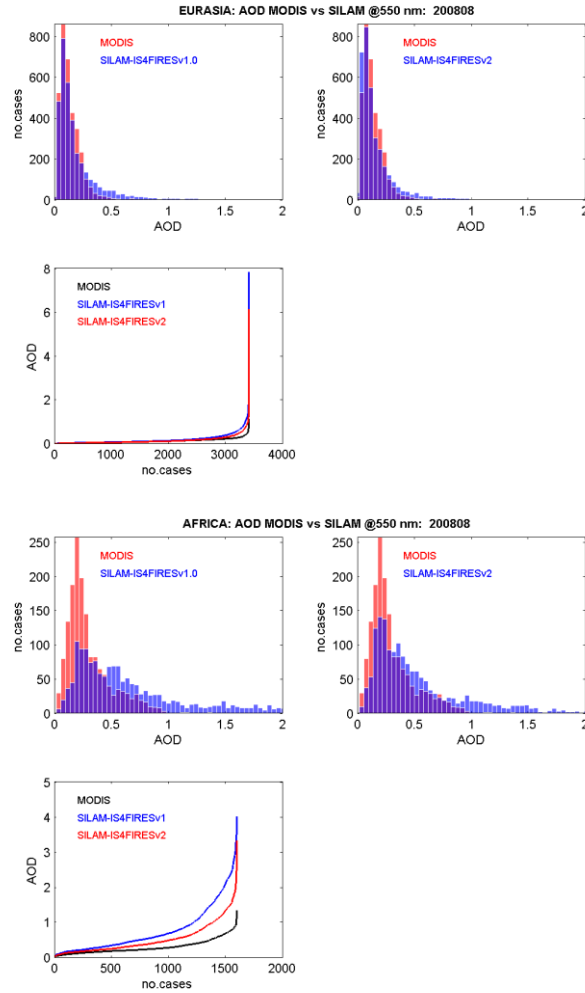


Figure 28. Histograms and cumulative distribution for fire dominating cells (daily averages) for Eurasia and Africa in August, 2008: AOD predicted (MODIS) and computed with fire emissions estimated